



Hydrothermal iron oxide-Cu-Au (IOCG) mineralization at the Jalal-Abad deposit, northwestern Zarand, Iran



Behzad Mehrabi^{a,*}, Behrouz Karimishahraki^a, David Banks^b, Adrian Boyce^c, Bruce W.D. Yardley^b

^a Geochemistry Department, Faculty of Earth Sciences, Kharazmi University, Tehran 15719, Iran

^b SEE, University of Leeds, Leeds LS2 9JT, UK

^c Isotope Geology Unit, Scottish Universities Research and Reactor Centre, East Kilbride, Glasgow Gs75 0QU, UK

ARTICLE INFO

Keywords:

Jalal-Abad deposit
Fluid inclusion
Stable isotopes
LA-ICP-MS
IOCG deposit
Central Iran

ABSTRACT

The Jalal-Abad iron oxide ± Cu ± Au ± Bi ± Co deposit is hosted in Early Cambrian volcanosedimentary units (CVSU) of the Kashmar–Kerman zone, Central Iran. Magnetite is the main ore mineral at depth and is associated with Na–Ca rich alteration, dominated by actinolite. Magnetite compositions (EPMA) are very low in TiO₂ (0.03–0.07 wt%), V₂O₅ (0.02–0.06 wt%) and CoO (0.01 to 0.42 wt%). At intermediate to shallow levels potassic alteration is associated with chalcopyrite, pyrite, arsenopyrite, cobaltite, bismuthinite and gold. The mineralization occurs in massive, breccia matrix, open space filling, disseminated and vein-like styles. Gold occurs as small inclusions (< 50 μm) within chalcopyrite and pyrite. The δ³⁴S values of pyrite at Jalal-Abad vary from 4.7 to 22.8‰ with an average of 12.7‰ (CDT) indicating more than one source of S, including evaporites, and minor mixing with magmatic sulfur. The δ¹⁸O values of magnetite are 1.0–6.4‰, with an average of 3.4‰ consistent with precipitation from magmatic-hydrothermal fluids. The δ¹³C values of dolomites are between –5 and –11‰ (PDB), while the δ¹⁸O values varies from 13.6 to 14.3‰, indicating hydrothermal dolomitization. Multiphase fluid inclusions in quartz from the iron ore stage (L + V + S) are abundant with homogenization temperatures of 220–480 °C. Salinities vary between 32 and 53 wt% NaCl equivalent. Laser-ablation inductively-coupled-plasma mass spectrometry (LA-ICP-MS) analyses performed on individual fluid inclusions hosted by quartz indicate significant concentrations of Fe and Cu, up to 16,076 and 3204 ppm with an average of 6914 and 792 ppm respectively. Ca/K values for fluid inclusions are 0.53–8.68 with an average of 1.75 indicating mixing of magmatic and non-magmatic fluids. Our proposed model for the Jalal-Abad deposit is that during the Early Cambrian gabbro-diorite magmas intruded the sedimentary sequence and provided magmatic constituents and a heat source for hydrothermal processes. Stable isotope, microthermometry and chemistry of fluid inclusions suggest that both magmatic and basinal fluids play a role in the mineralization.

1. Introduction:

The IOCG deposits have been recognized as a distinct class since the discovery of the Olympic Dam deposit, South Australia, and the geological features of this group of deposits has been summarized by Hitzman et al. (1992). IOCG deposits comprise a distinct class of hydrothermal polymetallic deposits that may also be associated with deposits of Kiruna-type (IOA), (Hitzman, 2000; Groves et al., 2010). IOCG deposits have high economic potential comprising low-Ti magnetite and/or hematite, Cu and Au. Ore bodies are structurally controlled and commonly occur as breccias, veins, stockworks or massive lenses, commonly associated with sodic or sodic-calcic alteration (Hitzman, 2000; Pollard, 2001; Williams et al., 2005; Groves et al., 2010). Iron oxide-apatite deposits that are not associated with Cu ± Au

mineralization are termed IOA deposits (Williams, 2010a). The majority of IOCG deposits occur in Paleoproterozoic volcanosedimentary sequences and exhibit earlier iron and later Cu–Au mineralization (Rieger et al., 2010). IOCG deposits are enriched in iron oxide, Cu, Au, LREE and may contain some other metals such as U, Ag, and Zn with economic potential (Groves et al., 2010). The origin of trace metals in IOCG deposits may be related both to ultramafic to mafic mantle-derived magmas (such as Co and Ni) and to leaching of metals such as Zn and U from a large volume of crustal material (Hitzman and Valenta, 2005). The complexity of magmatism accompanying IOCG deposits (ranging from ultramafic-mafic to felsic plutons) can be explained by mixing of magmas derived from the mantle with felsic magmas generated by underplating of continental crust (Hart et al., 2004). The ore-forming fluids for IOCG mineralization have been variously proposed to

* Corresponding author.

E-mail address: mehrabi@khu.ac.ir (B. Mehrabi).

<https://doi.org/10.1016/j.oregeorev.2019.01.019>

Received 11 August 2018; Received in revised form 14 January 2019; Accepted 21 January 2019

Available online 31 January 2019

0169-1368/ © 2019 Elsevier B.V. All rights reserved.

be nonmagmatic, magmatic or hybrid magmatic-nonmagmatic (Williams et al., 2005; Hunt et al., 2007).

The Poshtebadam-Bafgh-Zarand district in central Iran is a world class iron oxide province. Overall this region contains over two billion tons of iron ore reserves (NISCO, 1980) with more than 80 major magnetic anomalies and deposits in an area of 7500 km² (Förster and Jafarzadeh, 1994; Jami, 2005; Daliran et al., 2009; 2010; Bonyadi et al., 2011; Stosch et al., 2011). The main iron oxide deposits of the Poshtebadam-Bafgh-Zarand district include Chador-Malu (400 Mt; Torab and Lehmann, 2007), Se-Chahun (140 Mt; Bonyadi et al., 2011), Choghart (216 Mt; Torab and Lehmann, 2007) and the Jalal-Abad (200 Mt; Technoexport, 1976). These deposits comprise massive magnetite and magnetite-apatite ore hosted in Early Cambrian sequences of sedimentary and volcanic rocks (lavas, pyroclastic and epiclastic rocks). The origin of the Poshtebadam-Bafgh-Zarand iron oxide deposits has been debated for some decades and different ore genesis models have been proposed. Some investigators proposed a magmatic origin comparable to Kiruna-type iron oxide-apatite ore deposits (Förster and Jafarzadeh, 1994; Daliran, 2002; Moore and Modabberi, 2003; Jami et al., 2007; Torab and Lehmann, 2007; Bonyadi et al., 2011). Other propose that the ores are hydrothermal, formed by metasomatic replacement of volcanic rocks by iron leached from preexisting rocks (Haghipour, 1974, Daliran, 1990, 1999, and 2002). Hydrothermal fluids played an important role in formation of the magnetite-apatite deposits in Bafgh region. The close temporal and spatial association of Early Cambrian felsic volcanic rocks and iron oxide deposits suggest that felsic magmatism and mineralization were contemporaneous (Daliran, 1990; Daliran et al., 2009, 2010). The Bafgh iron district is associated with abundant apatite, often rich in REE, so the ores are referred to as iron oxide-apatite (IOA) deposits (Daliran et al., 2009). Other REE-rich minerals such as monazite, xenotime, bastnasite, urtite, thorite, davidite and bertholite have been reported (Jami, 2005; Torab and Lehmann, 2007; Deymara et al., 2018). The Jalal-Abad iron ore deposit is located in the southeast of the Poshtebadam-Bafgh-Zarand mining district, 38 km northwest of Zarand town in Kerman province, Iran (Fig. 1). Previous studies are restricted to an unpublished report (Technoexport, 1976). According to Technoexport (1976), Jalal Abad deposit contains 200 Mt of iron ore with an average composition of 45% Fe, 1.18% S and 0.08% P. Gold and copper were not reported from the Jalal-Abad area, until our preliminary studies (Karami Shahraki and Mehrabi, 2016). In the Poshtebadam-Bafgh-Zarand district most of the iron mines (Chador-Malu, Choghart, Se-Chahun, etc) contain magnetite-apatite-REE and are associated most commonly with albite and actinolite (Daliran et al., 2010; Bonyadi et al., 2011; Stosch et al., 2011). They contain minor chalcopyrite (Bonyadi et al., 2011), but gold has not yet been reported. In the Narigun, veins high in U, Ni, Co, Ag and As were formed by hydrothermal fluids associated with sericitization and carbonatization of wall rocks (Gharsi and Karimi, 2011). The Jalal-Abad deposit, in contrast to other iron deposits in the Poshtebadam-Bafgh-Zarand district, is associated with Cu-Au ore. The Jalal-Abad deposit is similar to the Se-Chahun and Choghart deposits in terms of its iron mineralization (magnetite as the main ore mineral) and alteration (association with actinolite and chlorite), but also contains minor apatite and more abundant sulphide minerals. The deposit is currently mined by IMPASCO (Iran Minerals Production and Supply Co). In this paper we point out similarities between the Jalal-Abad deposit and iron rich deposits that are classed as IOCG. We present field characteristics, mineralogy, fluid inclusion microthermometry, fluid chemistry and stable isotope data for the iron oxide mineralization at Jalal-Abad and associated hydrothermal alteration, trying to understand the genesis of the ore and possible source of ore bearing fluid.

2. Methods

Ore minerals and alteration assemblages were initially identified in core samples by optical microscopy. Thin sections (n = 40), polished

thin sections (n = 20) and polished sections (n = 40) were prepared for petrographic studies. Major element analyses of bulk samples were performed using XRF (X-ray fluorescence) at the Iranian Mineral Processing Research Center (IMPRC). Trace elements were determined by inductively coupled plasma mass spectrometry (ICP-MS) at the Acme Analytical Laboratories (Vancouver) Ltd, Canada. Fluid inclusion microthermometry was performed on double-polished wafers using a Linkam THMSG 600 heating-freezing stage at the Iranian Mineral Processing Research Center (IMPRC). The precision of the temperature measurements was less than $\pm 1^\circ\text{C}$ for heating and $\pm 0.3^\circ\text{C}$ for freezing. The microthermometry stage was calibrated using synthetic fluid inclusion standards for the critical point of pure H₂O (374.1 $^\circ\text{C}$), pure H₂O (0 $^\circ\text{C}$) and the freezing points of pure CO₂ (-56.6 $^\circ\text{C}$). Reproducibility of calibrations are $\pm 0.2^\circ\text{C}$ for freezing and $\pm 0.6^\circ\text{C}$ for heating, based on replicate measurements of n-Hexane (melting point: -94.3 $^\circ\text{C}$) and cesium nitrate (melting point: +414 $^\circ\text{C}$), for freezing and heating, respectively.

Magnetite, quartz and dolomite were separated and analysed for oxygen and carbon stable isotopic composition at the Scottish Universities Research and Reactor Centre, Scotland. Scanning electron microscope (SEM) studies (by FEI Quanta 650 FEG-ESEM), sulfur stable isotope analysis and LA-ICP-MS analysis of fluid inclusions were carried out at the School of Earth and Environment, University of Leeds, UK. X-ray diffraction analyses (XRD) were performed on a Philips Xpert-pro model using Co K α 1 (1.789010 \AA) radiation, monochromator on secondary optics, 40 kV power and 35 mA current at IMPRC. Mineral analyses were obtained by a CAMECA SX100 electron probe microanalysis (EPMA) with 5 wavelength dispersive spectrometers at IMPRC. Operating conditions for major elements were; accelerating voltage of 15 kV, beam current of 20nA, beam size of $\sim 5\mu\text{m}$ and 15 s counting time. Trace elements were measured at an accelerating voltage of 25 kV, a beam current of 20nA, beam size of $\sim 3\mu\text{m}$ and 30 s counting time. Gold was analyzed under a beam diameter of 1 μm with an acceleration voltage of 25 kV and 100nA current. Detection limits for major and minor element are approximately 0.05 wt% and 0.01 wt%, respectively. Standards used for Zn, Ag, As, Co, Te, Bi, Mn and Sb calibration were sphalerite, argentite, gallium arsenate, pure cobalt, hessite, pure bismuth, rhodonite and antimonite, respectively. The following standards were also used; chalcopyrite for Cu, Fe and S, wollastonite for Si and Ca, Fe₂O₃ for Fe, corundum for Al and native gold for Au calibration. Standards used for Ti, V, Mg, Ni and Cr were rutile, vanadinite, periclase, nickel oxide and chromite, respectively. Raw data were corrected for matrix effects using the ZAF correction procedure implemented by CAMECA.

3. Regional geologic setting

The central Iran plate is a Gondwana fragment, juxtaposed with other fragments during the Alpine-Himalayan orogeny, and is divided by large regional faults into three major crustal domains. From west to east these are the Yazd, Tabas and Lut blocks (Alavi, 1991). The Yazd and Tabas blocks are separated by the Kashmar-Kerman tectonic zone (Fig. 1). This zone extends for 600 km in length and is 80 km width (Ramezani and Tucker, 2003). The Poshtebadam-Bafgh-Zarand district is located in the central and southern sections of the Kashmar-Kerman Zone and comprises more than 34 iron ore anomalies and deposits which host over 2 Gt of iron oxide ore (NISCO, 1980; Torab and Lehmann, 2007; Stosch et al., 2011; Bonyadi et al., 2011). The Jalal-Abad iron deposit is situated in the southeastern part of this zone (Fig. 1). The Kashmar-Kerman structural zone is defined by fault trends. The northern part of the zone is defined by the northeast Poshtebadam, Kalmard, Uzbek-kuh and Kashmar faults and the south part is outlined by the northwest Kuhbanan and Zarand faults (Ramezani and Tucker, 2003). Within the Kashmar-Kerman Zone, rocks ranging from Neoproterozoic metamorphic basement to Quaternary sediments are exposed.

Early Cambrian volcanosedimentary units (CVSU) are exposed

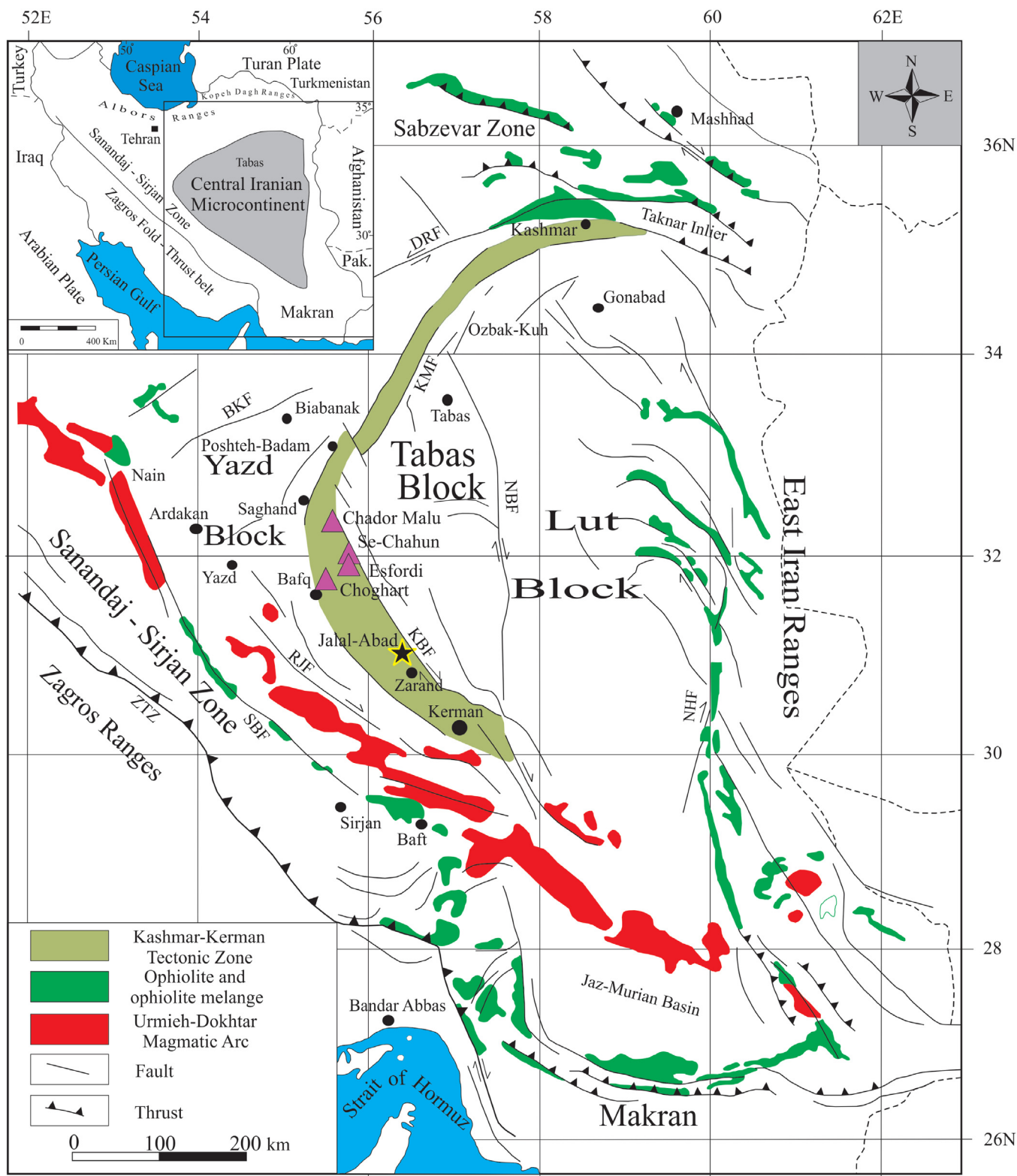


Fig. 1. Structural map of Central Iran showing the location of iron ore mine (modified after Ramezani and Tucker, 2003). The Poshtebadam-Bafgh-Kerman district iron province is part of the Kashmar-Kerman zone. BDF = Behabad Fault, BKF = Biabanak Fault, CHF = Chapedony Fault, DRF = Doruneh Fault, KMF = Kalmard Fault, MAF = Mehdiabad Fault, KBF = Kuhbanan Fault, MBF = Minab Fault, NHF = Nehbandan Fault, RJF = Rafsanjan Fault, SBF = Shahre-Babak Fault, TKF = Taknar Fault, UZF = Uzbak-Kuh Fault, ZRF = Zarand Fault, ZTZ = Zagros Thrust Zone.

throughout the Poshtebadam-Bafgh-Zarand area (Ramezani, 1997; Ramezani and Tucker, 2003) and host the most important iron oxide-apatite-REE-Th-U (Daliran, 2002; Daliran et al., 2009), Fe-Mn and SEDEX Zn-Pb (Rajabi et al., 2015) deposits in the area. Compositions of

the volcanogenic rocks vary from felsic to mafic and include rhyolitic, rhyodacitic, agglomeratic and spilitic lava and diabase. The sedimentary rocks include dolomites, dolomitic limestones and evaporites (Haghipour and Pelissier, 1977; Ramezani and Tucker, 2003). In

Central Iran these sequential series have been termed the Rizu and Desu series, Esfordi or Saghand Formation in different parts of the area between Poshtebadam and Kerman (Huckriede et al., 1962; Haghypour, 1977; Samani, 1993). Daliran (2002) proposed that in the southern part of the Bafgh region, the lower volcanic unit of Early Cambrian age had a continental to epicontinental affinity dominated by felsic tuffs while the upper unit is dominated by dolomite which indicates a shallow marine sedimentary environment. Zircon U-Pb dating of rhyodacite in CVSU unit in the Bafgh region yielded a minimum age of 528 ± 1 Ma (Ramezani and Tucker, 2003).

In the Poshtebadam-Bafgh-Zarand area, intrusive bodies ranging in composition from granite-granodiorite to gabbro-diorite are intruded into the Upper Precambrian metamorphic rocks and the Early Cambrian volcanosedimentary unit (CVSU, Ramezani and Tucker, 2003). U-Pb dating of zircon in the Zarigan, Douzakh-Darreh and Sefied granites yields an age of 526 ± 3 Ma (Ramezani, 1997). A proposed tectonic setting for the Poshtebadam-Bafgh-Zarand region during the Early Cambrian is crustal extension associated with intra-continental rifting (Berberian and King, 1981; Talbot and Alavi, 1996; Samani, 1998). The rifting event is associated with alkaline magmatism and is characterized by alkaline volcanic rocks and alkaline granites (Samani, 1988, 1998; Daliran, 1990, 1999, 2002; Förster and Jafarzadeh, 1994). Based on geochemical studies of the igneous and metamorphic rocks from the Poshtebadam-Bafgh, Ramezani and Tucker (2003) proposed that the Kashmar-Kerman zone was an active continental margin magmatic arc in the Early Cambrian.

The Zarand region contains the thickest and most complete sequence of Neoproterozoic and lower Paleozoic rocks in Iran and the Middle East. A rift model, involving horst and graben formation, has been invoked to account for the patterns of shallow marine platform facies in the Late Precambrian to Silurian sequences of the study area (Berberian and King, 1981; Hamed, 1995). Neoproterozoic rocks are dominant on the west side of the Kuhbanan fault while Paleozoic and Mesozoic units occur to the east. The Morad series is the oldest unit in the area and consists of unmetamorphosed Neoproterozoic clastic rocks, sandstone, shale and sandy shale with green to grey colors (Huckriede et al., 1962).

4. Geology of the Jalal-Abad deposit

4.1. The ore-hosting Early Cambrian volcanosedimentary unit (CVSU)

The Jalal-Abad deposit is hosted by the Early Cambrian volcanosedimentary unit. Tuff and ignimbrite with rhyodacitic composition and rhyodacite lavas are widespread in the central and southeastern part of the area although dolomite units host a small part of the ore and contain hydrothermal quartz, magnetite and hematite as veins, veinlets and in disseminated form. Host rocks of the Jalal-Abad ore body include sandy siltstone, dolomite and felsic volcanic rocks (Fig. 2). In the east and along the Kuhbanan fault, the CVSU unit contains a large amount of gypsum in a dolomitic sequence. The volcanic rocks in the mineralized zone are extremely altered and secondary minerals such as magnetite, actinolite, chlorite or a quartz-pyrite-sericite assemblage preserve ghost remnants of volcanic textures. The igneous activity in the Jalal-Abad is bimodal, with felsic volcanic rocks, small mafic intrusive bodies and diorite and gabbro dykes (Figs. 2, 3a and b). Locally diorite and gabbro at Jalal-Abad exhibit equigranular to porphyritic textures which have been altered to chlorite and sericite. Early Cambrian volcanosedimentary rocks are intruded by diorite and gabbro sills or dykes (Fig. 3c and d).

4.2. Orebody

The ore body is lens-shaped, extending along a NW trend located in an area of open folding. The length of the ore body based on the magnetic anomaly is approximately 2500 m. In the Jalal-Abad deposit,

iron oxide-Cu-Au \pm Bi-Co mineralization is identified mainly from borehole samples. The cross section of the deposit (Fig. 3) is based on exploratory drill cores which demonstrate iron mineralization down to 486 m below the surface with variable oxidation depending on topographic situation and fault displacements. The surface outcrop of iron ore is limited to the northwestern part. Rocks immediately below the deposit are chloritized sandstones with veins and veinlets containing quartz, chlorite, calcite, dolomite (minor ankerite) and/or pyrite, without any iron oxide mineralization. Medium- and fine-grained euhedral and subhedral pyrite occur in this sandstone, disseminated in a chloritic alteration assemblage. The ore bearing horizon is 250–180 m thick and consists of chloritized siltstone, sandy siltstone, rhyodacitic tuff and dolomite with iron oxide and sulfide mineralization. Above the ore body are siltstone, sandstone, conglomerate, rhyodacitic ignimbrite, rhyodacitic tuff, dolomite, breccia and alluvium. There is no iron oxide mineralization in this upper zone. Analyses of 10 samples from drill cores are given in Table 1. Variations in chemical composition mainly reflect the variable mineralization of the analyzed samples. Total Fe_2O_3 and SiO_2 contents range from 15 to 86.70 and from 4.73 to 48.53 wt%, respectively, reflecting variable amounts of magnetite and silicate minerals. MgO and CaO are in range of 1.13–24.48 and 0.14–8.01 wt%, respectively, indicating part of mineralisation in dolomite. P_2O_5 varies from 0.01 to 0.7 wt%. V and Zr vary from 35 to 80 and 1 to 44.70 ppm, respectively. Cu and Au vary from 3.20 ppm to 1.30 (CuO) wt % and < 0.01 to 27.2 ppm, respectively. Cu-rich samples have the highest Au content. Four types of orebodies have been recognized based on chemical composition and iron grade (Technoexport, 1976): (1) oxidized (2) magnetite-rich (3) magnetite-poor and (4) mineralized siltstone (Table 2). The average grade of Cu in these four iron ore types is variable, ranging from 0.15% in oxidized ore to 0.9% in mineralized siltstone. The mineralization is locally controlled by NE-SW trending faults and N-S and E-W trending faults are less important (Fig. 4).

5. Hydrothermal alteration

Magnetite-bearing sodic and sodic-calcic alteration is the dominant alteration type in most IOCG systems. Copper, gold and other metals may be precipitated during potassic alteration. A number of IOCG deposits contain late, structurally high-level zones of hydrolytic alteration characterized by the replacement of earlier alteration assemblages by martite (hematite after magnetite), sericite, carbonate minerals, and quartz (Hitzman et al., 1992; Williams et al., 2005; Groves et al., 2010). In the Jalal-Abad deposit alteration shows a general transition from sodic-calcic (actinolite rich) at deeper levels, potassic (K-feldspar + biotite) at intermediate levels and sericitic and silicic alteration (sericite + quartz) at very shallow levels. X-ray diffraction, petrography and electron probe microanalysis (EPMA) indicate that the common alteration minerals assemblages are sodic-calcic alteration, potassic alteration, dolomitization, silicic alteration. The hydrothermal alteration around the deposit is controlled by NW trending faults adjacent to dioritic sills and dykes.

5.1. Na-Ca alteration

The earliest hydrothermal alteration at the Jalal-Abad is predominantly sodic-calcic alteration which is characterized (Fig. 5a) as massive, vein-type, spotty and disseminated actinolite. This alteration is particularly common in deep levels (c. 450 m) and formed during iron oxide stage mineralization in association with magnetite, pyrite, apatite and minor amounts of zircon. Dolomitic host rocks are altered to actinolite and display a replacement texture in some section of deposit (Fig. 5b). sodic-calcic alteration is poorly developed at contacts with dolomite sequences where only minor actinolite, talc and epidote are present. Talc commonly occurs as fine-grained aggregates. In the deep levels, chlorite and talc commonly replace actinolite in later stages. Chlorite alteration is widespread in both host rocks and mineralization

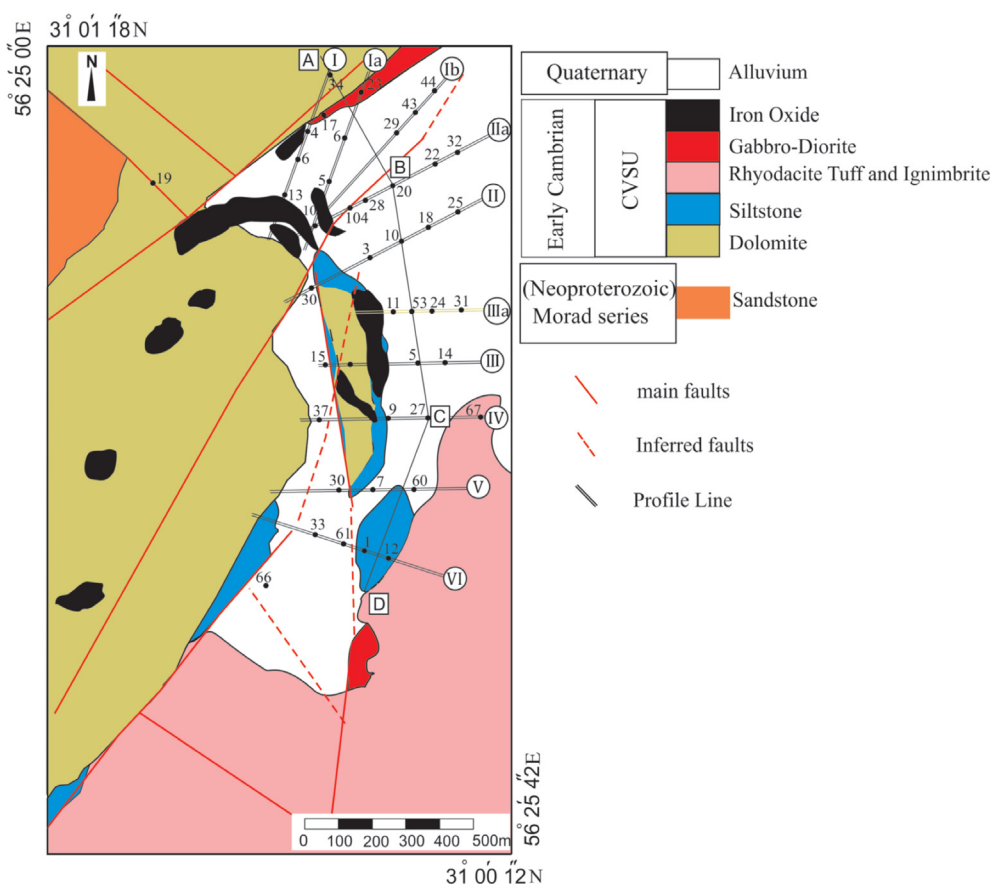


Fig. 2. Geological map of the Jalal-Abad deposit (modified after Technoexport, 1976).

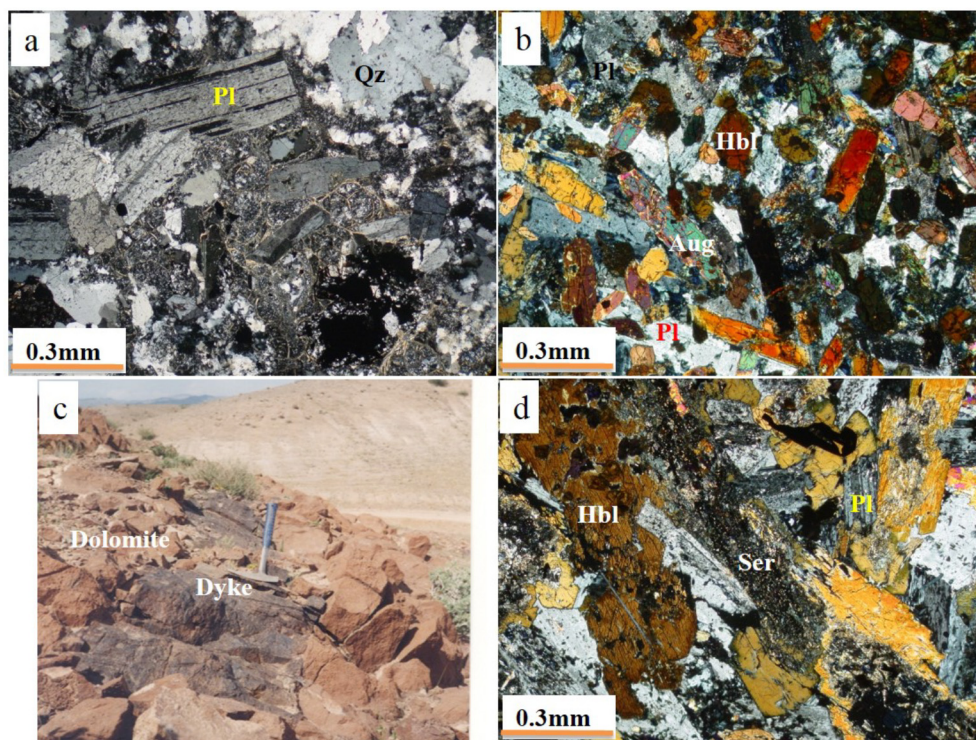


Fig. 3. Photomicrographs of volcanic and intrusive rocks in the Jalal-Abad deposit; a) rhyodacite with plagioclase phenocrysts and quartz crystals in glass and fine grained groundmass; b) gabbro intrusion with relatively small plagioclases, amphibole and pyroxene; c) diorite dyke which has been emplaced into the dolomite (CVSU) and d) Photomicrographs of diorite dyke with large plagioclases and amphibole. Plagioclases were replaced by chlorite and sericite. All abbreviations after Whitney and Evans (2010): Pl: plagioclase, Qz: quartz, Hbl: hornblende, Aug: augite, Ser: sericite.

Table 1
Major and trace elements composition of drill cores from the Jalal Abad deposit.

Sample No.	1	2	3	4	5	6	7	8	9	10
Bore hole No.	KB11	KB10	KB11	KB11	Z20	Z53	Z44	162	Z23	Z32
Depth (m)	376	251	425	415	320	147	494	168	114	479
Major elements	(%)									
Fe ₂ O ₃	86.70	17.3	84.16	72.33	29.71	57.64	67.35	60.21	15.00	63.32
SiO ₂	9.75	48.56	4.73	13.56	41.47	15.87	15.85	19.92	47.70	20.98
Al ₂ O ₃	0.09	2.27	0.11	0.30	3.44	7.36	2.73	0.89	6.41	0.51
MgO	1.13	24.48	2.45	8.66	19.77	12.55	8.91	12.49	16.02	11.82
CaO	1.47	0.47	2.54	0.33	0.40	1.02	1.39	1.53	8.01	0.14
MnO	0.02	0.02	0.05	0.01	0.01	0.04	0.04	0.05	0.13	0.01
K ₂ O	0.03	0.08	0.03	0.04	0.04	0.06	0.80	0.07	2.08	0.04
Na ₂ O	0.05	0.09	0.04	0.09	0.05	0.03	0.09	0.09	0.23	0.03
P ₂ O ₅	0.03	0.19	0.01	0.08	0.02	0.70	0.09	0.07	0.13	0.04
CuO	0.26	n.d	1.30	0.07	n.d	0.13	n.d	0.64	0.02	n.d
TiO ₂	0.01	0.12	0.01	n.d	0.10	0.43	0.11	0.03	0.37	0.02
LOI	0.50	6.41	4.6	4.50	4.97	4.16	2.62	3.98	3.92	3.06
Total	100.04	99.99	100.03	99.97	99.98	99.99	99.98	99.97	100.02	99.97
S	0.16	1.98	1.52	3.12	0.04	0.71	0.04	2.92	0.11	0.04
Trace elements	(ppm)									
Cu	2072.00	29.37	> 10000	546.00	34.71	1073.00	3.20	5092.00	122.80	42.52
Au	0.02	n.d	27.20	8.90	n.d	n.d	n.d	0.80	n.d	0.01
Ag	0.06	0.04	0.61	3.37	0.59	0.72	0.70	0.34	0.45	0.14
Mo	3.10	0.26	1.39	5.71	2.36	0.73	2.30	4.18	0.05	88.04
V	48	36	35	38	65	80	53	59	46	48
Sn	3.70	1.40	9.00	3.00	2.50	11.30	10.20	3.70	11.80	11.60
Zn	7.40	12.90	47.40	11.30	7.60	17.60	20.30	6.30	28.60	10.00
Pb	1.49	5.27	1.24	3.27	213.40	4.15	1.76	15.93	3.79	21.09
Ba	3	2	2	2	2	3	12	4	13	2
Ni	8.00	21.80	10.20	78.60	5.10	34.70	6.10	41.60	27.80	25.30
Co	2.30	27.00	5.90	69.80	1.80	129.60	2.50	34.20	4.40	4.90
As	3.30	67.70	12.10	131.90	2.90	307.60	2.10	141.00	0.40	15.30
Bi	3.98	4.42	22.77	8.46	0.21	119.70	0.06	8.69	0.06	2.60
Te	1.58	0.57	10.79	4.17	0.57	0.27	0.05	0.12	1.51	0.22
W	9.80	0.80	1.40	1.50	2.20	22.80	5.40	20.80	1.50	30.80
Zr	1.00	20.60	0.90	1.40	8.30	40.70	11.50	6.30	33.00	1.50
Hf	0.02	0.39	0.02	0.02	0.19	1.80	0.32	0.14	1.08	0.02
Th	0.20	3.40	0.10	0.80	2.50	3.10	0.10	0.50	6.00	0.40
U	18.80	5.30	11.60	29.20	18.70	7.90	1.80	6.30	1.30	5.40
Nb	0.20	1.36	0.22	0.23	1.90	8.19	1.77	0.42	5.14	0.39
Ta	0.10	0.10	0.10	0.10	0.10	0.50	1.90	0.10	0.60	0.10
Nd	0.50	1.40	0.50	0.70	0.50	4.00	0.80	2.50	5.80	0.30
Sm	0.20	0.30	0.20	0.20	0.20	1.60	0.40	0.90	1.60	0.10
La	0.10	0.40	0.20	0.20	0.30	1.40	0.30	1.80	6.50	0.10
Ce	0.48	1.14	0.48	0.72	0.65	4.68	1.09	3.90	11.29	0.21
Eu	0.10	0.20	0.10	0.10	0.10	0.50	0.20	0.30	0.70	0.10

Table 2
Average chemical composition of the Jalal-Abad iron ore types (Technoexport, 1976).

Comp.	Oxide Ore	Magnetite rich Ore	Magnetite poor ore	Mineralized Siltstone
Fe	54.21	53.31	33.10	16.55
P	0.06	0.08	0.08	0.10
S	0.42	1.50	1.53	1.35
FeO	5.04	22.60	16.01	10.68
SiO ₂	11.36	12.29	24.04	43.60
Al ₂ O ₃	1.10	0.78	2.10	3.32
MgO	2.63	4.63	6.01	8.20
CaO	3.39	2.30	4.25	5.20
MnO	0.18	0.07	0.26	0.80
Cu	0.15	0.17	0.16	0.90
Fe/FeO	13.41	2.35	0.06	1.54
TiO ₂	0.12	0.11	0.22	0.20

zones. In volcanic and intrusive rocks, amphibole and plagioclase are altered to chlorite and epidote (Fig. 5c, d and e). The chlorite alteration is associated with pyrite in sandstone and siltstone which occurs as dissemination and late stage veins.

5.2. Potassic alteration

Potassium silicate alteration is present in this deposit and is represented by biotite and K-feldspar in felsic volcanic rocks (Fig. 5f and g). The potassic alteration may form by alkali exchange in rocks with moderate K₂O contents (Hitzman et al., 1992). It is not well developed at deep levels but is abundant at moderate to shallow levels.

5.3. Sericitization and silicification alteration

The final stage of hydrothermal alteration is distinguished by sericite, quartz, muscovite and hematite. The Cu mineralization is also associated with hematite-chlorite-sericite to intense hematite-quartz alteration. Plagioclase and K-feldspar in felsic volcanic rocks are replaced by clay minerals and sericite (Fig. 5h). This alteration is common in surface outcrops and at shallow levels and is mostly associated with malachite mineralization. Silicification is in the form of veins and vugs of quartz in magnetite ore and host rocks (Fig. 8i). Veins of quartz, pyrite, magnetite, hematite, chalcocopyrite, calcite and dolomite occur in sandstone and siltstone hosts in the footwall of the deposit and in dolomite outcrop.

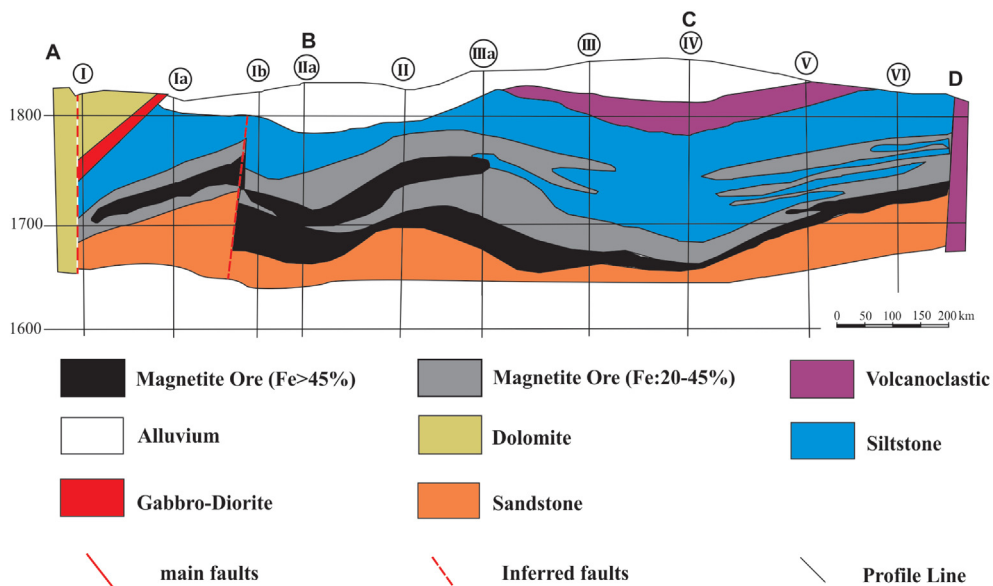


Fig. 4. Geological cross section of the Jalal-Abad iron ore deposit (modified after Technoexport, 1976).

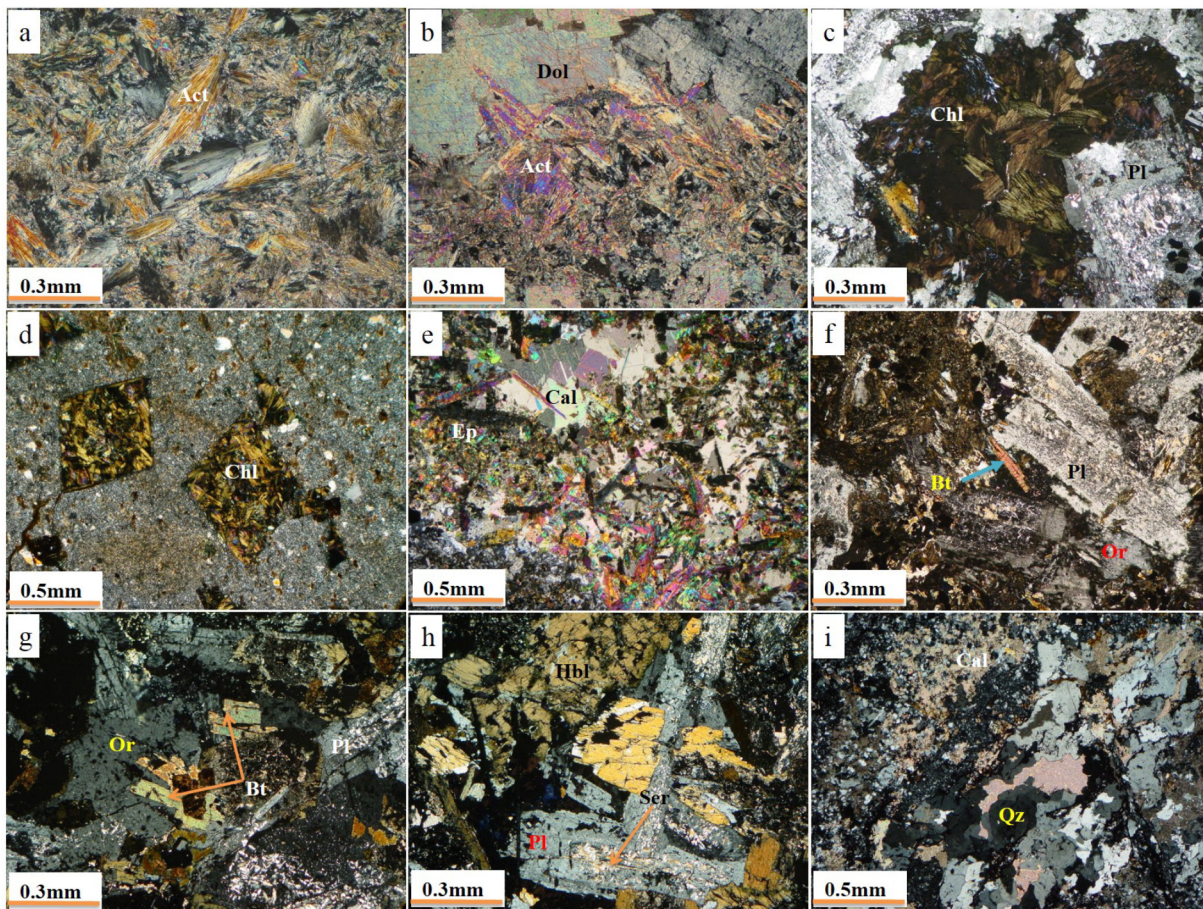


Fig. 5. Photomicrographs of hydrothermal alteration in the the Jalal-Abad deposit; a) Ca-Na metasomatism with actinolite (Act) in magnetite ore body (drill core 23, 440 m); b) replacement of actinolite in dolomite (dol); c) albite (Ab) altered to chlorite (Chl) in diorite (drill core 16, 122 m); d) amphibole crystals in felsic volcanic rock were generally replaced by chlorite and sericite (drill core 20, 152 m); e) carbonate-epidote (Ep)-chlorite alteration in diabase dyke (drill core 16, 135 m); f and g) Biotite (Bt) and orthoclase (Or) in potassic alteration in felsic volcanic rocks; h) sericitized (Ser) and chloritized plagioclase crystal in dioritic intrusion (drill core 16, 120 m) and i) quartz and calcite as infill of altered samples in felsic volcanic rocks (drill core 31, 63 m).

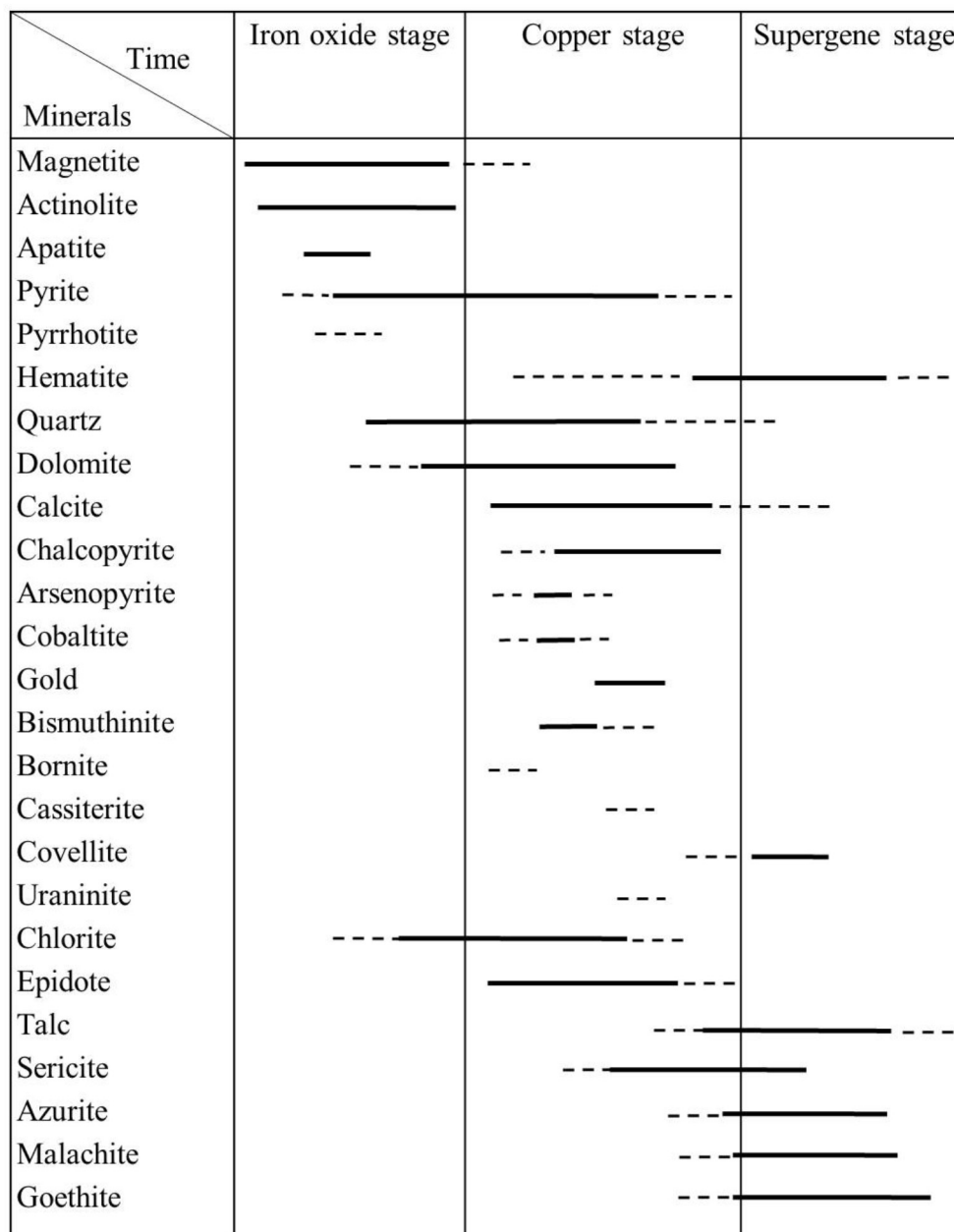


Fig. 6. Paragenetic sequence of iron oxide Cu-Au mineralization in the Jalal-Abad deposit.

5.4. Ca-alteration stage

The Ca-alteration stage is distinguished by minerals such as dolomite, calcite and epidote replacing or overprinting earlier minerals. Petrographic studies show that dolomites formed as very fine to medium crystalline masses outside the ore deposit (west of the Jalal-Abad deposit) but as coarsely crystalline dolomite and saddle dolomite in the mine pit, and adjacent to the iron ore bodies. Very fine to medium crystalline dolomite are replacement features formed during early diagenesis of the CVSU (Mehrabi et al., 2015). Recrystallization of these primary dolomites (very fine crystalline to medium crystalline), dissolution of the matrix dolomites, and formation of coarse and Saddle dolomites are related to hydrothermal processes and fault activities (Mehrabi et al., 2015). Saddle dolomite is normally associated with magnetite and occurs as veins and open space fillings.

6. Mineralization

The history of alteration and mineralization at Jalal-Abad has been divided into three stages; an early iron oxide stage, copper stage and late supergene stage (Fig. 6). The Jalal-Abad deposit mainly comprises iron oxides (magnetite, ± hematite), pyrite, chalcopyrite, and malachite, occurring in massive, brecciated (Fig. 7a), open space filling (Fig. 7b), disseminated and vein forms. Magnetite, hematite, pyrite and chalcopyrite recognized as dissemination in coarse crystalline and saddle dolomite (Fig. 7c).

6.1. Iron oxide stage

Massive Magnetite is the dominant ore mineral in lower part of the orebody (Fig. 8a) and is mainly associated with talc, chlorite, actinolite and dolomite (Fig. 8b). Magnetite occurs mostly as subhedral grains ranging in size from 0.1 to 0.6 mm. The oxidation zone reaches down to

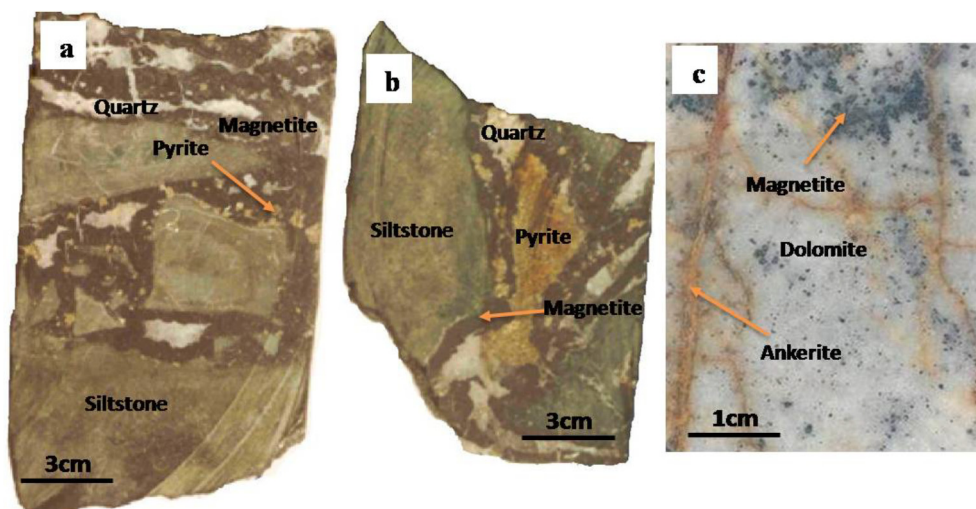


Fig. 7. Photographs of drill core samples from ore types in the Jalal-Abad deposit; Samples a and b were collected from boreholes 25 (depth 350–360 m) and samples c was gathered from boreholes 11 (depth 140 m) a) ore breccia type, brecciated siltstone space filled by magnetite, pyrite and quartz b) open space filling of magnetite, pyrite and quartz in siltstone; c) disseminated magnetite in hydrothermal dolomite (saddle dolomite).

150 to 200 m depth and depend on intensity of martitization. Hematite (martitization) mostly occurs near the surface and along fractured zones, and formed as a supergene mineral due to magnetite oxidation (Fig. 8c); it is rare at depth. Magnetite relicts remain in secondary hematite indicating incomplete martitization (Fig. 8d). The martitization of magnetite accompanied potassic and sericitic alteration. Goethite and other hydrous Fe oxide minerals are absent at deeper levels and

only occur near the surface in the sericitic alteration zone. EPMA analyses of the magnetite indicate a very low TiO_2 (0.03–0.07 wt%), V_2O_3 (0.02–0.06 wt%), CoO (0.01 > to 0.42 wt%), NiO (0.01–0.03 wt %), Cr_2O_3 (0.01–0.04 wt%) and MnO (0.01–0.06 wt%) contents (Table 3).

Based on textural evidence, two types of pyrite can be recognized: early stage pyrite, in close association with magnetite as euhedral to

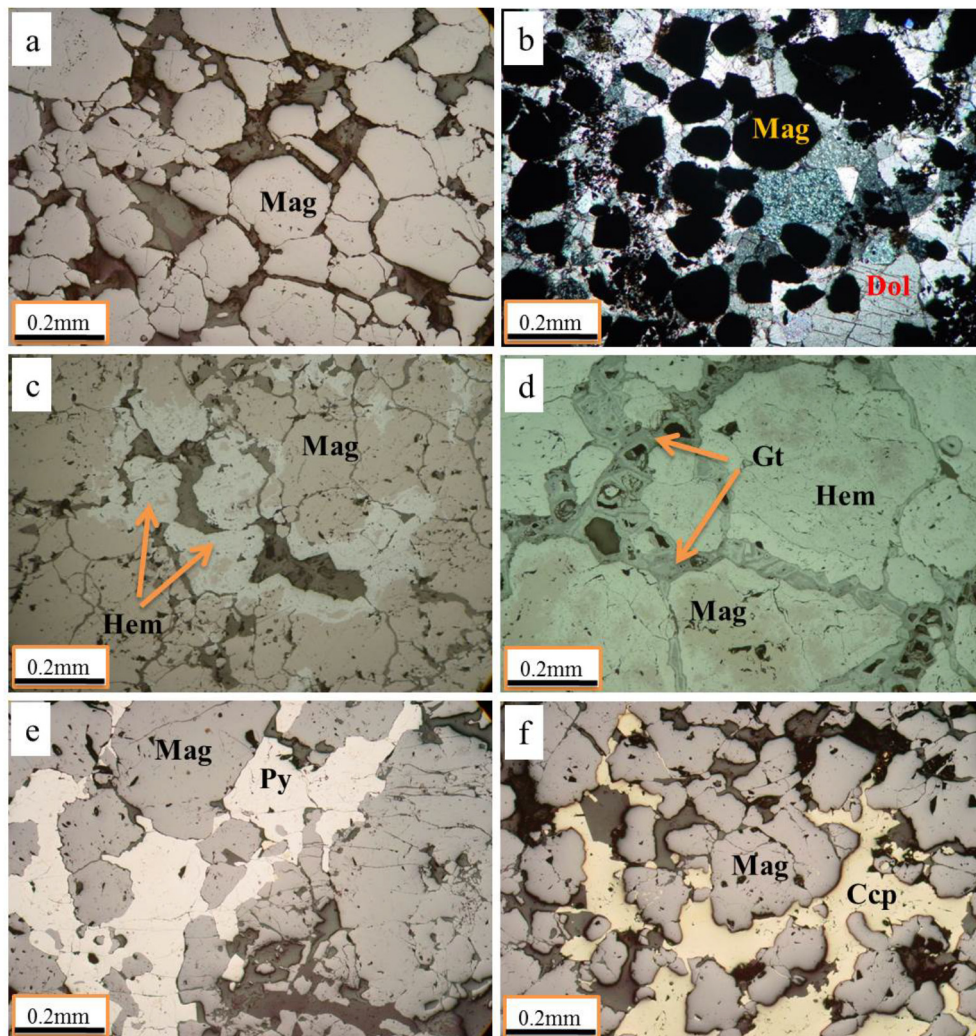


Fig. 8. Photomicrographs of the ore minerals in the Jalal-Abad deposit; a) massive magnetite (Mag) from rich magnetite ore zone with subhedral, anhedral and fragmented crystals (drill core 44, 565); b) disseminated of subhedral and anhedral magnetite in groundmass of dolomite (Dol) (drill core 11, 160 m); c) replacement of magnetite by hematite (Hem) in massive iron ore zone sample along the fractures (drill core 9, 221 m); d) Complete replacement of magnetite (Mag) by martite or secondary hematite (Hem) in oxide ore and hematite replaced by goethite (Gt) along margins, small magnetite relicts preserved in hematite (drill core 16, 79 m); e) subhedral and anhedral pyrite (Py) associated with coarse grain magnetite (drill core 44, 520) and f) magnetite space filled by chalcopyrite (Ccp) in ore zone sample during copper stage (drill core 44, 510).

Table 3
Electron probe micro analyses (EPMA) of magnetite from the Jalal Abad deposit.

	1	2	3	4	5	6	7	8	9	10	11	12	13
SiO ₂	0.18	0.65	0.39	0.23	0.02	0.05	0.07	0.14	0.11	0.18	0.07	0.11	0.15
TiO ₂	0.03	0.06	0.04	0.04	0.06	0.04	0.05	0.04	0.04	0.06	0.05	0.06	0.04
Al ₂ O ₃	0.04	0.01	0.03	0.01	0.03	0.01	0.04	0.03	0.03	0.04	0.06	0.04	0.04
V ₂ O ₃	0.04	0.02	0.03	0.04	0.04	0.05	0.03	0.05	0.03	0.02	0.04	0.05	0.05
FeO	30.43	30.89	30.37	30.55	29.6	32.03	39.78	31.22	39.77	30.27	39.9	31.22	30.65
Fe ₂ O ₃	68.43	68.49	68.27	68.52	69.17	67.78	69.03	68.12	69.00	69.04	69.04	68.55	68.99
MgO	0.01	0.06	0.05	0.02	0.02	0.03	0.02	n.d	0.01	0.05	0.04	0.06	0.04
CaO	0.17	0.20	0.06	0.21	0.18	0.29	0.12	0.2	0.13	0.17	0.11	0.35	0.14
MnO	0.02	0.02	0.02	0.04	0.01	0.01	0.02	0.01	0.02	0.01	0.01	0.02	0.03
CoO	0.39	0.00	0.30	0.28	1.36	n.d	n.d	n.d	n.d	0.47	n.d	n.d	0.01
NiO	0.01	0.03	0.02	0.02	0.01	0.02	0.02	0.01	0.01	0.03	0.01	0.02	0.01
ZnO	0.01	0.00	0.01	0.00	0.01	0.00	0.07	0.01	n.d	0.02	0.02	n.d	0.04
Cr ₂ O ₃	0.02	0.03	0.02	0.01	0.02	0.01	0.02	0.02	0.01	0.01	0.02	0.01	0.02
Total	99.78	100.45	99.62	99.96	100.14	100.31	100.27	99.84	100.15	100.36	100.38	100.49	100.19
	14	15	16	17	18	19	20	21	22	23	18	24	25
SiO ₂	0.47	0.44	0.6	0.05	0.64	0.79	0.12	0.68	0.66	0.5	0.12	0.51	0.87
TiO ₂	0.06	0.07	0.03	0.07	0.06	0.06	0.05	0.06	0.04	0.06	0.05	0.07	0.03
Al ₂ O ₃	0.04	0.02	0.03	0.01	0.03	0.02	0.01	0.02	0.04	0.01	0.01	0.05	0.02
V ₂ O ₃	0.03	0.04	0.06	0.03	0.02	0.04	0.05	0.03	0.03	0.04	0.04	0.04	0.04
FeO	30.65	30.92	31.01	30.46	30.43	30.61	30.63	30.6	30.48	30.75	31.01	29.57	30.57
Fe ₂ O ₃	68.28	68.29	68.09	68.45	68.37	68.23	68.45	68.33	68.57	68.47	69.02	68.84	68.11
MgO	0.02	n.d	0.04	n.d	0.01	0.04	0.08	0.07	0.01	0.06	0.01	0.03	0.07
CaO	0.08	0.18	0.22	0.24	0.21	0.11	0.15	0.22	0.10	0.31	0.13	0.08	0.11
MnO	0.02	0.02	0.01	0.02	0.03	0.06	0.02	0.04	0.02	0.02	0.01	0.04	0.01
CoO	0.09	0.23	n.d	0.31	0.36	n.d	n.d	n.d	0.27	n.d	n.d	0.42	n.d
NiO	0.01	0.02	0.01	0.01	0.02	0.01	0.01	0.01	0.03	0.01	0.02	0.01	0.02
ZnO	0.02	0.03	0.03	0.03	n.d	n.d	0.03	n.d	0.08	n.d	n.d	n.d	0.01
Cr ₂ O ₃	0.01	0.02	0.02	0.01	0.04	0.01	0.02	0.01	0.02	0.01	0.02	0.01	0.02
Total	99.78	100.28	100.15	99.69	100.21	99.97	99.63	100.07	100.34	100.24	100.43	99.68	99.87

Table 4

Summary of electron microprobe results for ore minerals from the Jalal Abad deposit, data in wt. %. n.a: not analyzed, (n): number of analyses: 1) pyrite; 2) chalcopyrite; 3) arsenopyrite; 4) bismuthinite; 5) cobaltite; 6) tesomoite.

	1(10)	2(10)	3(9)	4(10)	5(10)	6(6)
S	52.85	35.10	17.75	19.17	19.5	4.01
Fe	46.52	30.33	31.99	0.43	2.49	1.50
Ni	0.03	n.a	0.01	n.a	0.12	n.a
Cu	0.07	34.34	0.02	0.28	0.03	0.97
Zn	0.02	0.01	n.a	n.a	0.02	n.a
As	0.38	0.09	46.98	0.02	43.46	n.a
Te	0.01	0.01	n.a	n.d	n.a	34.62
Bi	n.a	0.04	n.a	79.47	n.a	57.63
Ag	0.02	0.02	0.01	n.a	0.01	0.02
Au	0.03	0.01	0.01	n.a	n.a	n.a
Co	0.05	n.a	3.13	0.22	33.95	n.a
Sb	n.a	n.a	0.09	0.14	n.a	n.a
Total	99.98	99.96	99.99	99.73	99.58	98.75

subhedral grains (Fig. 8e) and late stage pyrite, commonly occurring as veinlets and open space filling formed in the copper stage. EPMA results of early stage pyrite show that the As content varies from 0.12% to 0.76% with an average of 0.38% and Cu contents vary from 0.02% to 0.27% with mean of 0.07% (Table 4). Au contents of pyrite vary from 0.01% to 0.08% with a mean of 0.03%. Apatite occurs as small grains in association with magnetite, actinolite and chlorite at deep levels (Fig. 9a). Small amounts of pyrrhotite are associated with magnetite at deep levels.

6.2. Copper and gold stage

The copper stage of mineralization varies with depth. At deeper levels chalcopyrite has filled the space between magnetite grains (Fig. 8f). Cu ore is disseminated through magnetite or occurs in veins. Chalcopyrites from rim and fractures are replaced by covellite. The Cu-Au ores occur in the potassic alteration zone. Gold is mainly associated

with copper sulphides and gold-bearing chalcopyrite veins generally crosscut the early stage pyrite. Native gold was detected as grains smaller than 50 µm in late stage pyrite (Fig. 9b) and chalcopyrite (Fig. 9c and 9d). EPMA analyses show that visible gold contains Ag between 4.24 and 6.78 wt% (Table 5). Accessory ore minerals include arsenopyrite, cobaltite, bismuthinite and uraninite (Fig. 9h) and occur as open space and fracture filling. Arsenopyrite, bismuthinite and cobaltite show intergrowths with each other (Fig. 9e). Bismuthinite mostly occurs as open space filling in magnetite fractures (Fig. 9f). The Co content of arsenopyrite generally varies from 1.81% to 5.74% with an average of 3.13% and Sb contents vary from 0.02% to 0.11% with mean of 0.09% (Table 4). EPMA analyses indicate that in some samples, bismuthinite is accompanied by a small amount of tesomoite (BiTe) (Fig. 9i). The bismuthinite normally contains 78.53%–80.36 wt% Bi and Co contents vary from 0.01% to 0.67% with mean of 0.22% (Table 4). Cobaltite (Fig. 9g) contains 33.95 wt% Co, 43.46 wt% As, 19.5 wt% S and 2.49 wt% Fe. Malachite and azurite replace chalcopyrite at a late stage.

7. Fluid inclusion study

Microthermometric data have been obtained from fluid inclusions hosted in hydrothermal quartz and dolomite from the iron oxide stage. The quartz samples for studying the fluid inclusions are from veins selected from drill cores while dolomite (saddle type) samples were collected from both the mine pit and drill cores (Fig. 7a, 7b and 7c). Samples are hosted by iron oxide mineralization and their association with mineralization is well established. Primary, pseudosecondary, and secondary inclusions have been identified according to the criteria of Roedder (1984) and Wilkinson (2001) and the main studies were performed on primary inclusions. Three types of fluid inclusion have been recognized in quartz and dolomite. Type I: three phase fluid inclusions (L + V + S) contain an aqueous phase, minor vapor bubble and some solids with an average inclusion size of 15 µm diameter (Fig. 10a and b). Type I inclusions are the most abundant and homogenize into the liquid phase. Some inclusions contain polysolids and in addition to

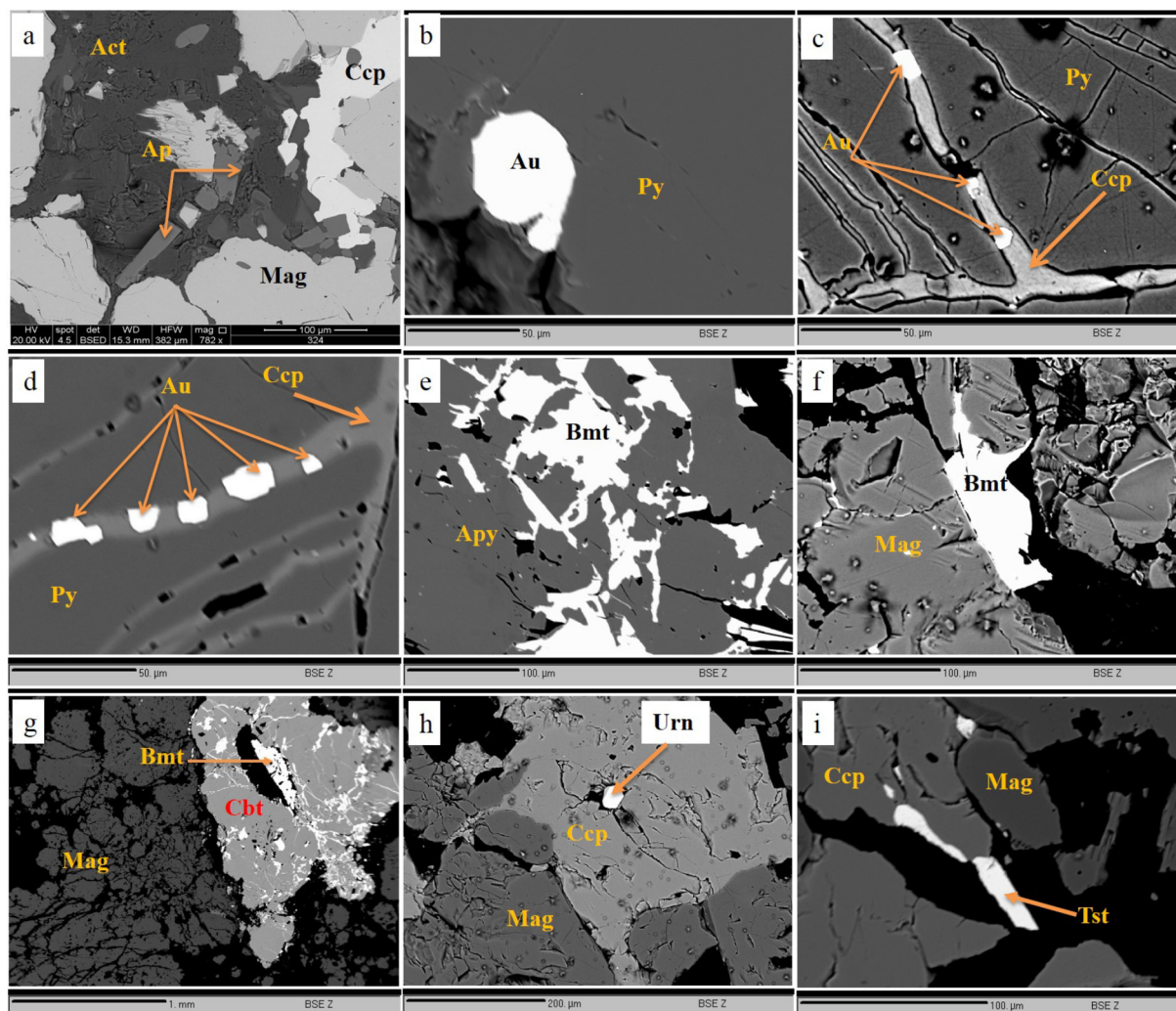


Fig. 9. Back-scattered electron (BSE) images demonstrating textural relationships between minerals in the Jalal-Abad ore bodies; a) chalcopyrite formed as space filling in matrix of magnetite, actinolite (Act) and apatite (Ap) (drill core 23, 460 m) b) Large rounded gold inclusion (50 μm) in sulfide-rich orebody as cavity filling (drill core kb11, 426 m); c & d) Chalcopyrite veinlets in pyrite containing gold grains of up to 20 μm (Au) within chalcopyrite veinlets in sulfide-rich orebody. The presence of gold grains in chalcopyrite veinlets represents the association of gold and copper mineralization, gold has been deposited during the copper mineralization stage (drill core kb11, 421–424 m); e) Intergrowth of arsenopyrite (Apy) with bismuthinite showing their simultaneous growth in copper stage (drill core 32, 460 m); f) Open space, cavity and fractures filling of bismuthinite (Bmt) in magnetite (drill core 32, 483 m); g) Intergrowth of cobaltite (Cbt) with bismuthinite as open space filling in magnetite (drill core 32, 455 m); h) Small uraninite (Urn) crystal formed as space filling in chalcopyrite (drill core 23, 450 m) and i) Intergrowth of tesomite (BiTe, Tst) with chalcopyrite in copper stage (drill core 32, 465 m).

Table 5

Electron probe micro analyses (EPMA) of visible gold grains within chalcopyrite veinlets in sulfide-rich ore body (drill core kb11, 421–424 m).

	1	2	3	4
Au	93.79	92.83	93.51	93.48
Ag	6.68	6.74	4.24	6.78
Cu	0.08	0.040	0.42	0.06
Fe	0.16	0.24	0.30	0.27
As	n.d.	0.04	n.d.	0.05
S	0.11	0.05	0.05	0.10
Total	100.87	99.95	98.52	100.74

halite, rounded and irregular shaped daughter crystals were interpreted as likely to be sylvite (Fig. 10c). Type II: (L + V) liquid-rich (80–95 vol %) aqueous inclusions are with minor vapor bubble (Fig. 10d). The majority of type II inclusions homogenize into liquid phase. Type III: CO₂-rich vapor inclusions are found mostly in dolomite samples. Secondary fluid inclusions are smaller than 4 μm in size and are mostly Type II two phase inclusions (L + V).

The homogenization temperatures (T_h) of Type I fluid inclusions hosted in quartz range from 220 °C to 480 °C, mainly falling between 250 °C and 350 °C (Fig. 11a) and salinity ranges between 31 and 52 wt% NaCl equiv. (Fig. 11b). Type I inclusions in dolomite are 5–25 μm in size with homogenization temperatures of 170 °C–305 °C (Fig. 10a) and salinity of 32–42 wt% NaCl equiv. (Fig. 10b). Type II fluid inclusions are common in dolomite and homogenize into the liquid phase between 155 and 308 °C. Final ice melting temperature is in range of –8 °C to –4 °C, indicating a salinity of 6–11 wt% NaCl equiv. In type III fluid inclusions, solid carbon dioxide melts ($T_m \text{CO}_2$) at –57 °C to –59.4 °C indicating the presence of only small amounts of other volatile components such as CH₄ or N₂ in the CO₂ (Thiéry et al., 1994).

8. LA-ICP-MS analysis of individual inclusions

Laser-ablation inductively-coupled-plasma mass spectrometry (LA-ICP-MS) is a powerful technique for analysing the elemental composition of single fluid inclusions in minerals (Shepherd and Cheney, 1995; Heinrich et al., 2003; Stoffell et al., 2004; Allan et al., 2005; Graupner

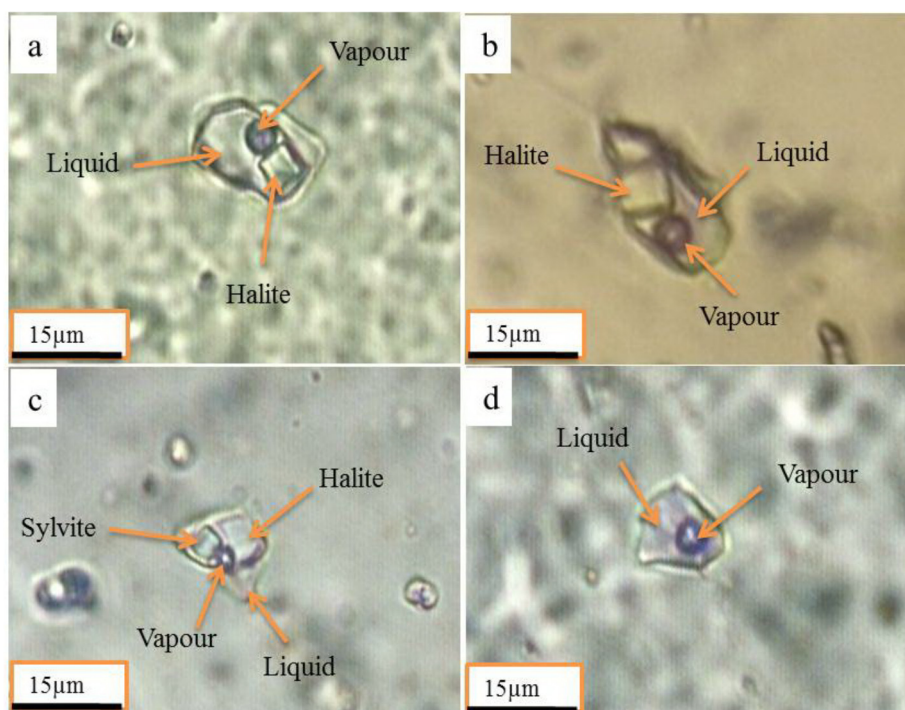


Fig. 10. Photomicrographs of quartz-hosted fluid inclusions in ore body; a & b) three phase halite-bearing fluid inclusions (L + V + S); c) multisolid (L + V + nS) fluid inclusions containing halite and sylvite daughter minerals and d) liquid rich fluid inclusion (L + V), type II.

et al., 2005). Chemical analysis of fluid inclusions hosted in ore stage quartz from the Jalal-Abad deposit was performed on 57 fluid inclusions with Li, Na, Mg, K, Ca, Mn, Fe, Cu, Zn, Sr, Ba, Pb concentrations determined using the procedures described in Allan et al. (2005). Data was processed using the SILLS software (Guillong et al., 2008). Note that chloride concentrations were estimated from microthermometry and charge balancing was used to convert the element ratios to Na, measured by LA-ICP-MS, to absolute concentrations. Individual ratios determined by LA-ICP-MS have large uncertainties, but averages of inclusions from distinct fluid inclusion assemblages are more robust. Chemical compositions of fluid inclusions by LA-ICP-MS analyses are shown in Table 6. The concentrations of Na and K are in the range 26,906–14,0716 ppm and 2372–70484 ppm respectively. Fe content varies from 576 to 16076 ppm with an average of 6914 ppm and Cu contents vary from 51 to 3204 ppm with mean of 792 ppm. The Na/Ca values for fluid inclusions vary from 0.38 to 37.51 with a mean of 3.79. The Ca/K ratios are 0.53–8.67 with an average of 1.75 (Fig. 12a). Magmatic fluids normally yield $K > Ca$, with Ca/K ratios of 0.01 to 1, whereas non magmatic fluids are often richer in Ca with Ca/K of 1–100 (Yardley et al., 2000; Yardley, 2005; Fisher, 2007; Gillen, 2010). The amounts of Fe and Cu in magmatic fluids can vary a lot, but are

commonly above 10,000 and 1000 ppm respectively, but depend on chlorinity (Fisher, 2007; Fisher and Kendrick, 2008; Gillen, 2010; Appold and Wenz, 2011). Mn concentrations are 424–7581 ppm, with an average concentration of 3645 ppm. Mn/Fe ratios range from 0.21 to 1.87 with an average of 0.60 (Fig. 12b). The average Sr/Na ratio in fluid inclusions is 0.034. Sr and Ba were released from limestone into solution during alteration (Appold et al., 2004; Appold and Wenz, 2011). The high salinity of the fluids is consistent with the high contents of K, Na, Ca, Mg, Fe, Cu, Mn, Li, Sr, Cs, Pb, Zn and Ba measured in the inclusions. The average magnesium concentration in the quartz-hosted fluid inclusions is 7974 ppm and average of Ca/Mg ratios in these fluid inclusions is 31.96. This ratio is in agreement with dolomitization (Appold and Wenz, 2011). Thus, the fluid responsible for precipitating iron ore in the Jalal-Abad may also have been responsible for dolomitization, which is consistent with the abundance of dolomite in the mining district.

9. Stable isotope study

Sulphur, oxygen and carbon isotopic compositions can provide specific evidence of fluid sources (Taylor and Sheppard, 1986; Zoheir

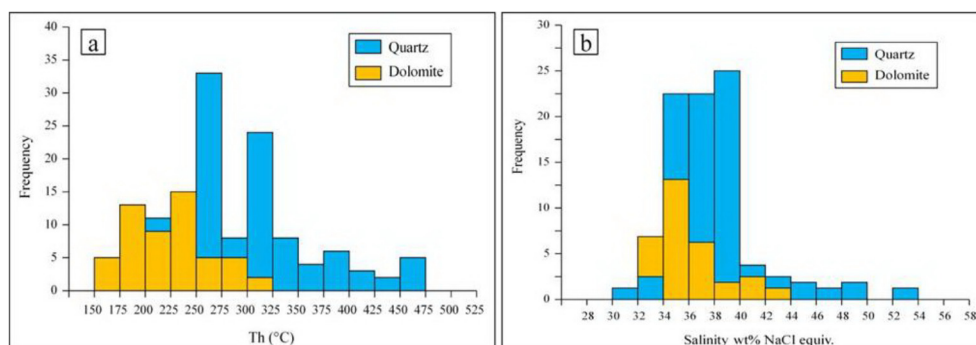


Fig. 11. Frequency distribution of homogenization temperatures (a) and salinity (b) of fluid inclusions in quartz and dolomite.

Table 6
Summary of LA-ICP-MS analyses of fluid inclusions (L + V + S).

Li	Na	Mg	K	Ca	Mn	Fe	Cu	Zn	Sr	Pb	Ba
103.21	45530.82	2823.42	56030.49	48540.94	2451.91	10057.99	205.64	504.88	2553.50	89.24	5450.36
156.91	69902.47	1964.78	25816.65	39581.51	3764.72	13550.91	428.25	890.86	1876.37	433.12	8655.48
105.31	46910.72	2125.41	46106.44	45742.46	6369.80	11455.42	643.05	1722.06	3358.80	453.13	14504.76
196.96	87736.98	699.07	23126.45	30886.39	5937.87	6413.46	1478.98	1096.73	2303.32	412.79	6526.60
174.96	77933.95	7895.88	24144.08	29097.62	3320.27	7989.86	1274.45	673.53	1362.05	275.58	5059.08
69.65	31024.30	6579.86	15063.20	81244.16	2116.41	3238.01	636.00	646.66	1701.19	940.05	5393.26
103.49	46093.94	679.94	44362.15	54066.84	5166.14	6164.38	274.80	1854.09	4481.41	778.42	13822.62
91.14	40591.23	482.67	70483.60	49760.03	3730.54	3890.05	1573.19	2112.20	2855.09	221.43	10523.12
118.74	52881.51	20111.07	24056.06	31366.60	3563.79	5097.53	396.84	511.50	2231.36	193.87	10307.28
422.56	48214.14	5042.48	39240.21	43843.11	5293.98	12237.86	558.51	1422.15	2366.27	445.15	12610.84
450.23	85566.39	214.57	36153.69	29803.43	1957.39	3947.08	671.08	971.49	2874.01	480.80	10313.99
205.73	39098.58	1331.35	63230.56	47152.02	3981.59	11485.80	3203.50	1476.17	2418.69	517.99	11446.46
221.95	42179.33	15680.81	15315.25	57123.54	1755.55	2366.29	252.21	506.69	1204.78	356.88	6278.86
582.25	110649.42	415.40	18351.58	18261.31	1492.02	5293.78	647.68	742.33	1398.66	246.10	4601.38
454.73	86413.98	4421.99	25648.19	25648.87	2785.04	5689.26	609.41	1158.64	2241.01	523.22	10940.03
597.58	113559.61	3553.32	14500.12	14577.09	1343.91	2945.67	310.81	581.23	871.83	221.81	5112.26
47.15	138910.77	1168.69	4260.58	6350.57	805.85	1523.57	51.27	153.90	378.69	104.12	1344.75
1074.50	74625.60	11290.28	30199.42	24151.39	1845.42	2987.14	1988.25	907.84	1756.37	337.35	7211.81
353.44	26906.52	1556.28	44705.37	67393.38	4962.00	11081.31	656.90	925.49	2104.24	156.71	11545.54
238.18	78027.34	480.86	22575.08	44070.39	3551.22	6151.69	319.03	1120.90	1378.26	396.08	1453.83
18.68	134925.41	2129.59	4260.87	674.96	8869.27	1087.10	56.47	152.25	251.20	38.93	1128.04
413.51	35770.58	7335.27	51620.13	48636.22	4497.05	8628.11	360.93	883.21	2932.86	322.48	10144.90
59.16	36190.15	157.50	17628.33	87486.01	2535.35	2939.68	77.03	607.65	1098.07	241.43	2253.99
438.32	31613.30	5079.43	37985.33	59654.67	6601.55	9408.85	615.61	1319.71	3578.13	743.37	11580.61
648.42	38313.52	5316.59	33493.60	56069.48	5169.66	9977.23	883.16	1805.78	3116.72	423.39	10108.16
1067.78	42259.84	16796.62	29682.49	40632.25	3442.89	5235.15	1149.13	736.17	2080.37	643.84	8340.54
598.14	67630.34	7403.30	30492.99	31574.74	3608.88	9890.52	674.61	1261.02	2078.04	384.09	7632.84
137.34	81607.98	3839.48	19815.29	35640.98	3401.56	5314.28	183.33	819.80	2361.47	369.40	1033.03
237.51	31941.56	4485.72	29137.05	64751.20	6928.26	8426.30	253.38	1825.12	4385.08	359.03	13953.19
951.64	45668.36	14628.53	31681.88	36078.12	3913.06	7418.28	1473.40	1771.99	1776.72	598.52	15077.76
503.03	85912.94	5485.81	10907.50	29809.06	2777.81	12978.33	823.66	574.33	888.26	324.54	2915.55
106.73	37901.81	15769.15	12775.62	52618.59	4416.63	6360.58	164.49	1600.41	3503.34	582.09	17155.67
1235.39	39863.29	7411.53	49429.45	39883.67	3373.66	12811.13	1294.92	1313.00	3197.97	339.07	13367.38
510.44	36661.37	24147.61	38381.63	28559.67	3305.92	8444.63	727.76	865.27	1452.35	377.52	8930.37
343.25	35754.80	8685.41	16640.53	61719.70	3840.28	15241.27	497.71	923.72	2390.00	141.23	5984.64
370.52	38595.47	17540.21	31579.21	42367.72	3326.71	4836.55	537.25	1286.67	1750.35	260.47	14260.04
294.46	30672.93	31818.47	6866.44	39299.62	4967.20	6298.14	426.97	862.74	1624.67	352.96	5367.22
228.55	84595.48	7230.13	24605.69	25058.12	2247.75	5038.62	1177.57	663.68	1314.23	154.22	11638.96
362.91	42895.48	11144.67	39469.43	43254.89	5330.96	7640.33	597.11	1385.41	2344.45	989.40	6924.39
2196.01	57161.67	8213.78	33731.43	36191.54	2729.93	5077.25	795.69	1909.78	1281.45	245.00	10877.82
776.51	59268.94	3883.89	35874.79	41645.71	3845.70	5887.29	825.02	1519.56	2643.98	564.80	14296.64
472.91	48948.01	134.61	52935.24	44466.35	3867.00	16075.81	681.36	835.29	2665.74	153.11	6395.32
615.04	64067.09	3225.34	36198.81	40920.31	3883.66	4444.54	891.81	900.24	3094.12	370.18	11314.84
294.87	54159.87	8195.05	26867.39	39801.14	5019.57	14018.63	753.91	1837.75	2981.37	958.56	7787.78
423.25	44088.86	1845.71	45697.77	47580.64	7580.88	11898.92	613.72	2681.25	3462.73	933.85	9206.95
1350.87	140716.01	386.97	2372.29	3751.44	426.77	608.32	1958.77	270.26	217.70	57.85	826.18
643.63	67045.12	2482.94	33939.49	37545.60	3972.12	6743.35	933.27	1172.95	2480.68	419.54	16304.39
1347.83	140398.96	386.10	2613.92	3937.72	424.15	575.63	1954.35	264.98	218.30	62.32	844.55
318.21	33146.67	16859.89	32641.39	48444.24	2970.92	6299.36	461.40	1324.36	2627.12	77.93	8246.89
453.87	47277.80	1454.92	41385.31	50172.31	7200.44	8461.54	658.11	1755.13	3661.03	405.50	11608.46
105.22	32889.94	20753.74	27224.80	41977.28	7441.87	5949.48	848.78	1525.63	3178.64	396.25	8554.09
1175.81	122480.59	7411.70	5607.22	6055.49	580.17	1070.33	1704.93	362.10	246.40	76.48	2267.21
366.86	38214.61	17279.73	39468.74	36003.60	4671.59	6295.89	645.40	3458.29	2118.68	547.81	12459.85
804.48	83799.85	2988.87	25301.85	29748.17	2650.33	7843.26	1166.49	959.94	1642.26	178.64	5945.65
418.22	43564.48	32508.38	26231.01	13860.20	2336.37	3958.37	606.42	1288.62	761.91	119.96	27644.40
549.93	57284.59	13704.33	5191.68	45063.71	2862.55	4791.96	797.40	1513.09	2367.03	269.05	14976.64
480.68	50070.53	26287.00	11208.79	26715.19	4756.20	2544.85	696.98	1731.21	2193.50	525.67	18965.28

et al., 2008; Sostaric et al., 2011; Johnson et al., 2012). Stable isotopes were also used to derive equilibrium temperatures for coexisting mineral pairs. Thirteen purified magnetite samples from different part of the orebody yielded $\delta^{18}\text{O}$ values from 1% to 6.4% (SMOW) with an average of 3.44% (Table 7). Carbon and oxygen isotopic studies were carried out on four hydrothermal dolomite samples associated with magnetite ore. The dolomite samples are depleted in $\delta^{18}\text{O}$ and $\delta^{13}\text{C}$ compared to original dolomite, with $\delta^{18}\text{O}$ between 15.53% and 19.54% (SMOW) and $\delta^{13}\text{C}$ from -7.65% (PDB) to -5.17% (PDB). Oxygen isotope analyses of nine hydrothermal quartz samples from ore bodies were also carried out. Hydrothermal quartz associated with magnetite shows $\delta^{18}\text{O}$ in range of 15.1–16.9% while quartz veins in the alteration zone are in the range 17.2–18.6%. $\delta^{34}\text{S}$ values are reported relative to

the Vienna Canyon Diablo Troilite (VCDT) standard. Handpicked pyrite samples were analyzed (5 pyrite samples from altered wall rock and 5 pyrites from mineralized zones) and the results display a wide range of $\delta^{34}\text{S}$ values from 4.7 to 22.8% (Table 7). This wide range probably indicates multiple S-sources, probably including evaporite sulphate, and magmatic sulphur from magmatic fluids or leaching of preexisting igneous sulfide minerals. It could also reflect fluid/rock interaction and/or oxidation. The light values of $\delta^{34}\text{S}$ are consistent with magmatic fluids or leaching of preexisting igneous sulfide minerals (Ohmoto and Rye, 1979; Ohmoto and Goldhaber, 1997), although other sources cannot be excluded.

The isotopic compositions of the mineralizing fluids were calculated based on temperature estimates from the average of homogenization

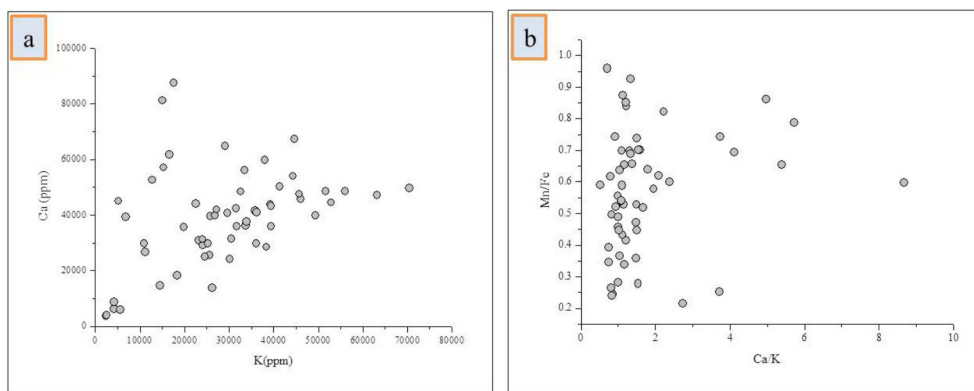


Fig. 12. Scatter plots of the concentrations of major cations in fluid inclusions hosted in quartz. a) Ca vs. K. and b) Mn/Fe ratios vs. Ca/K.

temperatures measured during microthermometric analyses of fluid inclusions and the equations of [Bottinga and Javoy \(1973\)](#) for quartz, [Matsuhisa et al. \(1979\)](#) for magnetite and [Horita \(2014\)](#) for dolomite. The isotopic composition of the mineralizing fluids ($\delta^{18}\text{O}_{\text{fluid}}$) at temperatures of 250–400 °C was 7.94–13.31 per mil ([Table 7](#)). According to [Taylor \(1986\)](#), the lower part of the $\delta^{18}\text{O}_{\text{fluid}}$ range partly coincides with magmatic fluids (5.5–10 per mil) and may indicate the presence of magmatic components in the hydrothermal fluid. The upper part of the range which typically has high $\delta^{18}\text{O}$ values suggests a possible interaction with sedimentary rocks ([Hoefs, 1987](#)).

10. Discussion

10.1. Mineralization features

Mineralization is multistage in the Jalal-Abad district. Disseminated magnetite ores, massive magnetite orebody and brecciated ores are the main forms of iron mineralization. Brecciated ores consist of angular

brecciated fragments of country rock (e.g., siltstone and tuff) cemented by magnetite and pyrite. Hematite and goethite ores formed in the supergene stage of mineralization. The earliest event was deposition of iron ore (magnetite, actinolite, pyrite, chlorite, and dolomite) and later mineralization is characterized by chalcopyrite, gold, arsenopyrite, cobaltite, bismuthinite, uraninite and tesomoite. In the Jalal-Abad deposit, Au mineralization is closely associated with Cu mineralization. The iron oxide orebodies are dominated by magnetite low in Ti and V. Copper is present as sulfides, carbonates and oxides in association with iron oxide, while Au occurs as inclusions in chalcopyrite, pyrite and magnetite. These characteristics are common features of IOCG deposits ([Hitzman et al., 1992](#); [Hitzman, 2000](#); [Williams et al., 2005](#); [Williams, 2010a](#); [Groves et al., 2010](#); [Zhao and Zhou, 2011](#)). In contrast with iron oxide-apatite (IOA) - REE deposits ([Daliran et al., 2009, 2010](#), [Stosch et al., 2011](#)) in the Bafgh district including Chadror-Malu ([Torab and Lehmann, 2007](#)), Se-Chahun ([Bonyadi et al., 2011](#)), Choghart ([Torab and Lehmann, 2007](#)) and Esfordi ([Jami et al., 2007](#)), the Jalal-Abad deposit is low in apatite and REE.

Table 7

Stable isotopic compositions of pyrite (Py), magnetite (Mag), quartz (Qtz) and dolomite (Dol) from the Jalal Abad deposit.

Sample	Drill core and location	Depth (m)	Rock type	T °C	$\delta^{18}\text{O}$ ‰ SMOW	$\delta^{18}\text{O}$ ‰ fluid	$\delta^{13}\text{C}$ ‰ V-PDB	$\delta^{34}\text{S}$ ‰ VCDT
KB2	KB2	297	Alteration zone					14.5 (Py)
KB5	KB5	150	Magnetite ore					6.2 (Py)
KB10a	KB10	240	Magnetite ore	350	3.2 (Mag)	10.69		5.7 (Py)
KB10b	KB10	251	Magnetite ore	350	2.4 (Mag)	9.89		4.7 (Py)
KB11a	KB11	259	Magnetite ore					9.3 (Py)
KB11b	KB11	301	Magnetite ore	400	6.4 (Mag)	13.34		22.8 (Py)
KB11c	KB11	316	Magnetite ore					9.1 (Py)
KB11d	KB11	422	Magnetite ore	400	2.6 (Mag)	9.54		12.5 (Py)
Z25a	25	348	Breccia zone	300	3.6 (Mag)	11.77		19.9 (Py)
Z32	32	315	Alteration zone					22.4 (Py)
KB11e	KB11	322	Magnetite ore	350	3.2 (Mag)	10.69		
KB11f	KB11	367	Magnetite ore	400	1 (Mag)	7.94		
Z29	29	120	Magnetite ore	300	2.6 (Mag)	10.77		
KB11g	KB11	295	Magnetite ore	350	4.5 (Mag)	11.99		
Z85	85	251	Magnetite ore	350	3.8 (Mag)	11.29		
Z32	32	250	Magnetite ore	300	4.6 (Mag);	12.77		
Z29	29	221	Magnetite ore		2.7 (Mag)			
KB5	B5	150	Magnetite ore		4.2 (Mag)			
Q2	North of mine		Quartz vein	350	15.5 (Qz)	10.21		
B38	38	321	Quartz vein	400	16 (Qz)	11.94		
B63	North of mine		Quartz vein		16.7 (Qz)			
Q8	North of mine		Quartz vein		16.5 (Qz)			
Q9	West of mine		Quartz vein	350	18.6 (Qz)	13.31		
Q10	West of mine		Quartz vein	300	18.0 (Qz)	11.14		
Q12	West of mine		Quartz vein	350	15.1 (Qz)	9.81		
Q13	North of mine		Quartz	350	17.2 (Qz)	11.91		
Z25a	25	348	Breccia zone	300	16.9 (Qz)			
Z11a	11	127	Dolomite	250	19.5 (Dol)	11.21	-4.17	
B63	North of mine		Dolomite	300	18.0 (Dol)	11.61	-7.21	
Z11b	11	95	Dolomite	250	17.9 (Dol)	9.58	-5.17	
Z11c	11	151	Dolomite	300	15.5 (Dol)	9.13	-7.65	

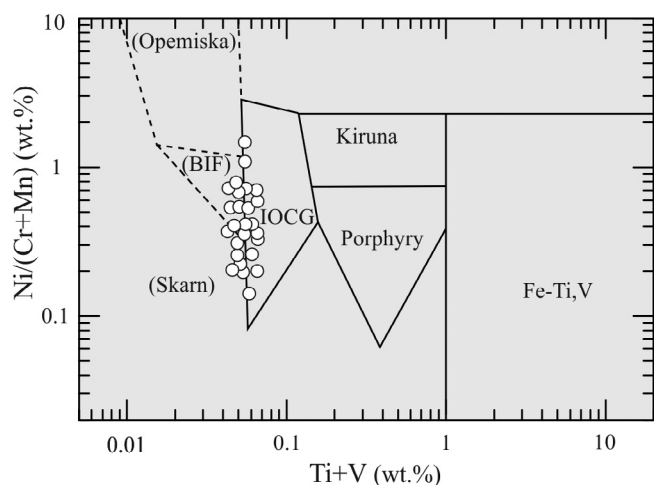


Fig. 13. Plots of V + Ti vs. Ni/(Cr + Mn) of magnetite in the Jalal-Abad deposit. Reference fields are after Dupuis and Beaudoin (2011).

The Jalal-Abad hydrothermal alteration system is characterized by early, sodic-calcic, potassic, chloritic, calcic, sericite, silicic and argillic alteration which in general is similar to the classical alteration system of IOCG deposits (Hitzman et al., 1992). The large-scale alteration at Jalal-Abad could have been genetically related to the gabbro-dioritic magmatism. Based on Vanko and Bishop (1982) the presence of actinolite in the magnetite ore indicates high temperatures for formation (greater than 400 °C). Actinolite is the most important silicate mineral present in the Bafgh iron deposits (e.g. Esfordi, Choghart, Chadour-Malu a Se-Chahun) and shows solid solution with tremolite (Torab and Lehmann, 2007; Bonyadi et al., 2011). Potassic alteration in the Bafgh district is marked by K-feldspar and biotite and was accompanied by leaching of REE from apatite (Torab and Lehmann, 2007). Most of the deposits in the Bafgh region have alkali alteration zones (sodic- and potassic alteration), which indicates a genetic link between Early Cambrian magmatism, alkali metasomatism and mineralization (Daliran et al., 2009, 2010).

Multistage hydrothermal events have been reported in other IOCG deposits such as Olympic Dam in Australia (Oreskes and Einaudi, 1990), Manitou Lake in Québec (Clark et al., 2005), Lala in China (Chen and Zhou, 2012) and Mantoverde district in northern Chile (Marschik et al., 2000; Rieger et al., 2010). The compositions of magnetite at Jalal-Abad are closely similar to magnetite in IOCG deposits (Fig. 13) with some overlap with BIF and skarn deposits (Dupuis and Beaudoin, 2011). The amount of TiO₂ in magnetite at Jalal-Abad is very low (0.03–0.07%) and similar to IOCG deposits (Hitzman et al., 1992). Although quartz is not abundant in IOCG deposits (Williams et al., 2005), it is locally abundant at the Jalal-Abad deposit and this is comparable to the Osborne Cu-Au deposit (Fisher and Kendrick, 2008). In the Bafgh district the late-stage fluids precipitated large amounts of calcite, quartz with minor to trace amounts of monazite, apatite and HREE minerals (Daliran et al., 2010).

Most IOCG deposits are hosted in metavolcanic and sedimentary rocks and associated temporally with igneous bodies (Hitzman et al., 1992; Hitzman, 2000; Williams et al., 2005; Williams, 2010; Groves et al., 2010; Hart et al., 2004; Pollard, 2006; Groves and Bierlein, 2007; Grainger et al., 2008). The Poshtebadam-Bafgh-Zarand district is part of the Kashmar-Kerman Zone volcanosedimentary-plutonic arc of early Cambrian age (Ramezani and Tucker, 2003). The arc is characterized by voluminous volcanic rocks from felsic to mafic in composition, sedimentary rocks (dolomites, dolomitic limestones, and evaporites) and plutonic complexes of granite through gabbro composition. During the early Cambrian, intrusive bodies were emplaced into volcanosedimentary rocks of the CVSU. Zircon (U-Pb) dating of the Zarigan, Douzakh-Darreh and Sefied granites by Ramezani (1997) yield an age of

526 ± 3 Ma. Age determination by the U-Pb method gave 507.3 Ma for the hornblende metasomatite ore in Saghand area (Samani, 1988). Apatite U-Pb dating of major IOA deposits in the Bafgh district by Stosch et al. (2011) indicate a mineralization age of 527–539 Ma which is in the age range bracket of felsic plutonic rocks from Ramezani, 1997 and Ramezani and Tucker, 2003. The magmatism is believed to provide heat and fluid components, and to drive the development of hydrothermal systems. The host rocks were affected intensely by hydrothermal alteration and mineralization. Hydrothermal alteration is controlled by permeability, fractures, shear and brecciated zones. Fluid circulation took place along the faults and through relatively permeable sandstone and siltstone in the lower part of the deposit. Copper-gold mineralization has been identified as forming under brittle conditions with low temperature alteration in most IOCG deposits (Monteiro et al., 2008).

10.2. Evolution of mineralizing fluids

Fluid inclusions that homogenize by halite disappearance are common in many porphyry copper, IOCG and other magmatic-hydrothermal ore deposits (Becker et al., 2008) and high-temperature, high-salinity fluids are believed to be responsible for Cu-Au mineralization in most IOCG deposits (Pollard, 2001; Pollard, 2006; Kendrick et al., 2007; Chen et al., 2011). Halite is a common daughter crystal of fluid inclusions in porphyry copper (Wilkinson, 2001; Wilkinson et al., 2009) and IOCG deposits (Becker et al., 2008) and is characterized by its cubic shape, refractive index and isotropic nature (Shepard et al., 1985). The wide range of homogenization temperature (170–450 °C), salinity (31–51 wt% NaCl equiv.) and ratios of K/Ca in fluid inclusions may indicate multiple fluid sources including both magmatic and basinal fluids (Yardley et al., 2000). Mn/Fe ratios in fluid inclusions show wide ranges (0.21–1.87) which indicate the presence of both reduced type and oxidized type fluids (Bottrell and Yardley, 1991). In oxidizing conditions specularite, hematite and martitization occurred while in the deeper parts of the system due to an increase in the redox state, magnetite and trace pyrrhotite were formed. The δ³⁴S values indicate that sulfur was derived mainly from seawater sulfate with minor mixing of magmatic sulfur. Seawater sulfur in hydrothermal deposits is usually attributed to an evaporite origin (Zhao and Zhou, 2011). In the Jalal-Abad area, evaporite sequences are associated with the Early Cambrian volcanic and sedimentary units (CVSU), which is consistent with evaporite origin for sulfur. The wide range of δ³⁴S values indicates mixing with magmatic fluids which may be the main source of metals for the iron oxide-Cu-Au mineralization. Fluid inclusion microthermometry of saddle dolomite from the Jalal-Abad deposit indicates high temperature and saline fluid are responsible for the deposition and recrystallization of saddle dolomites (Mehrabi et al., 2015). Saddle dolomites probably precipitate from mixing of hydrothermal fluids and dissolution of former dolomites (Mehrabi et al., 2015). The saddle dolomites in Jalal-Abad have δ¹³C values between –7.65 and –4.17‰ (V-PDF), indicate that carbon derives from deep-seated, possibly magmatic, and organic sources, whereas the δ¹⁸O vary from 15.5 and 19.5‰ (SMOW) point to a δ¹⁸O-rich, magmatic or sedimentary source (Schmidt et al., 2005; Ronchi et al., 2012). The IOCG deposits are closely associated with plutonic complexes and with broadly coeval fault systems. Stable isotope evidence indicates fluids and ore components were likely sourced from the intrusion (Sillitoe, 2003). Magmatic fluids cannot provide the sufficient energy for fracturing in host rocks, therefore mineralization is associated with fault activity, and in addition, the mixing of magmatic fluids with other fluids will led to the formation of ore (Sillitoe, 2003). The δ¹⁸O values of magnetite in El Laco and Mina Justa IOCG deposits are 3.6–4.6‰ (Rhodes et al. 1999) and 3.7–5.2‰ (Chen et al., 2011) respectively. In the Choghart iron oxide deposit (Bafgh, central Iran) δ¹⁸O values of magnetite are in range of 3.66 and 4.38‰, and related to magmatic-hydrothermal processes (Moore and Modabberi, 2003). The δ¹⁸O values of analyzed magnetite in the Jalal-Abad vary from 1 to

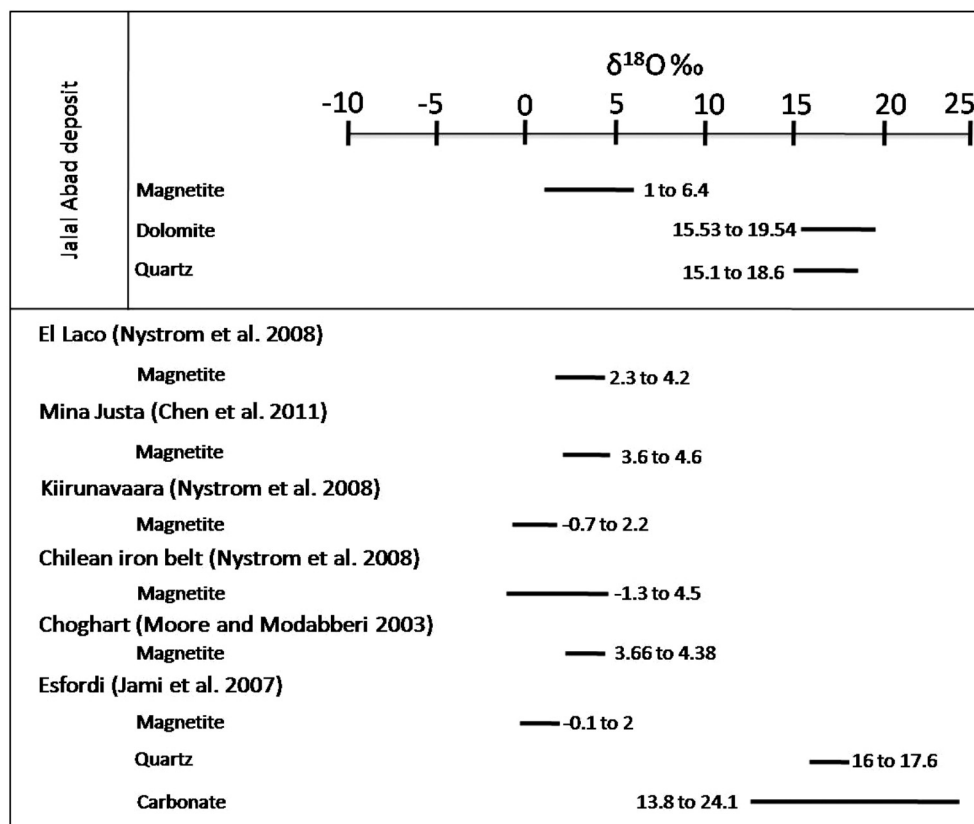


Fig. 14. Comparison of $\delta^{18}\text{O}$ data of magnetite, quartz, and dolomite in the Jalal-Abad deposit with other iron deposits worldwide.

6.4%, which are similar to those deposits (Fig. 14). In contrast, the $\delta^{18}\text{O}$ values of quartz are in the range of 15.1–18.4%, and might be modified by mixing with an ^{18}O -rich fluid or by interaction with wall rocks. The mixing of ^{18}O -enriched contact metamorphic fluid, arising from sediments metamorphosed by gabbro-diorite intrusions with primary hydrothermal fluid is a possible reason for heavy $\delta^{18}\text{O}$ values in quartz samples, but because of the high oxygen content of the wall rocks, direct re-equilibration of hydrothermal fluid and wall rocks for oxygen is also possible. Iron oxide-apatite deposits (IOA) in the Bafgh district occur in Early Cambrian volcanic and sedimentary units, possibly related to rifting, and iron oxide-apatite ores were formed during magmatic-hydrothermal condition (Daliran et al., 2009). Some iron deposits in the Kashmar-Kerman zone, including the Chador-Malu, Choghart, Se-Chahun, Chah Gaz, Mishdovan, Gasestan, North Anomaly and Lakkeh Siah deposits, are related to basic and ultrabasic intrusions (Jami et al., 2007; Bonyadi et al., 2011; Nabatian et al., 2015). The O and C isotope results for dolomite ($\delta^{13}\text{C}$ of -7.65 to -4.17% and $\delta^{18}\text{O}$ from 9.13 to 11.61%) indicate magmatic-hydrothermal fluids, or fluids equilibrated with a magmatic source for carbon and oxygen origin (Rieger et al., 2010; Johnson et al., 2012). The $\delta^{18}\text{O}$ composition calculated for the ore fluids (7.94–13.34%) suggests a magmatic or interaction with $\delta^{18}\text{O}$ -rich, possibly sedimentary rocks. The ranges of $\delta^{18}\text{O}$ fluid compositions for the Olympic Dam ranges from -2.5 to 10% (Oreskes and Einaudi, 1992) and some Australian Proterozoic IOCG deposits have $\delta^{18}\text{O}$ fluid compositions around 7–13% (Williams et al., 2005).

Three models have been proposed for IOCG deposits, involving magmatic-hydrothermal fluids, basin derived fluids and metamorphic fluids (Barton and Johnson, 2004). The mineralogical, microthermometry, chemistry of fluid inclusions and stable isotope data shows that magmatic-hydrothermal metal bearing fluids, nonmagmatic hydrothermal fluids and mixing of them are responsible for iron-Cu-Au mineralization in the Jalal-Abad deposit. The occurrence of native gold associated with chalcopyrite and high salinity fluid inclusions may arise

from co-transport of Cu and Au by Cl complexes (Rieger et al., 2010).

11. Conclusions

Several iron oxide deposits occur in the Poshtebadam-Bafgh-Zarand district, hosted by Early Cambrian volcanic and sedimentary units (CVSU), and these define an important iron metallogenic province in central Iran. Most contain significant amounts of apatite, but have negligible Cu mineralization and Au mineralization has not been reported; they are classified as iron oxide-apatite (IOA) deposits. However, in the Jalal-Abad deposit, economical Cu mineralization occurs in addition to iron oxide, and is accompanied by Au, Bi, Co, As, Te, Sn and Ba mineralization but apatite is insignificant. The Cu sulfides mostly formed under brittle conditions as disseminations and veinlets. Jalal-Abad is similar to many IOCG deposits. The ore deposit is structurally controlled and iron ore minerals are low Ti, V, Cr magnetite and hematite. Mineralization developed under reduced conditions at the beginning and it evolved toward relatively oxidized conditions. Hematite exists mainly in oxidation zones near the surface and diminishes between 150 m and 200 m as secondary origin, though primary hematite also is found in minor amounts. The large volumes of hydrothermal alteration surround the orebodies and occur localized along shear zones. The alteration types include sodic-calcic (albite, actinolite), potassic, sericite, quartz, and carbonate. The combinations of microthermometric, LA-ICP-MS data from individual fluid inclusions and stable isotopic compositions have provided insight into the evolution of the hydrothermal process that formed the Jalal-Abad iron oxide + Cu + Au deposit. The K, Fe, Ca, Na and Cu concentrations in fluid inclusions are most probably related to the mixing of magmatic and basinal fluids. Alteration and fluid-rocks interaction play important role in concentration of Ca, Na, Sr and Ba in fluids. Formation of IOCG deposit in the Jalal-Abad was likely related to the intrusion of mafic intrusive rocks, which are considered as a source of

heat and some fluids. Based on occurrences of halite crystals in fluid inclusions, metals probably were transported by Cl-rich fluids.

Acknowledgments

We would like to acknowledge the IMIDRO (Iranian Mines and Mining Industries Development and Renovation Organization) and IMPRC (Iranian Mineral Processing Research Center) for their financial supports. We gratefully acknowledge the support of the ICIOC (Iranian Central Iron Ore Co.) and the Jalal-Abad mine during sampling and field work. We would like to thank Dr. Farhaz Daliran and an anonymous referee for their careful, incisive and constructive reviews for through review and constructive comment. Special thanks are also due to Prof. Franco Pirajno for his dedicated editorial work

Appendix A. Supplementary data

Supplementary data to this article can be found online at <https://doi.org/10.1016/j.oregeorev.2019.01.019>.

References

- Alavi, M., 1991. Tectonic map of the Middle East, 1/5000000. *Geol. Surv. Iran*.
- Allan, M.M., Yardley, B.W.D., Forbes, L.J., Shmulovich, K.I., Banks, D.A., Shepherd, T.J., 2005. Validation of LA-ICP-MS fluid inclusion analysis with synthetic fluid inclusions. *Am. Mineral.* 90, 1767–1775.
- Appold, M.S., Numelin, T.J., Shepherd, T.J., Chenery, S.R., 2004. Limit's on the metal content of fluid inclusions in gangue minerals from the Viburnum Trend, southeast Missouri, determined by laser ablation ICP-MS. *Econ. Geol.* 99, 185–198.
- Appold, M.S., Wenz, Z.J., 2011. Composition of ore fluid inclusions from the viburnum trend, southeast Missouri district, United States: implications for transport and precipitation mechanisms. *Econ. Geol.* 106, 55–78.
- Barton, M.D., Johnson, D.A., 2004. Footprints of Fe-oxide (Cu-Au) systems: University of Western Australia, Centre for Global Metallogeny. *Spec. Publ.* 33, 112–116.
- Becker, S.P., Fall, A., Bodnar, R.J., 2008. Synthetic fluid inclusions. XVII.1 PVTX properties of high salinity H₂O-NaCl solutions (> 30 wt% NaCl): application to fluid inclusions that homogenize by halite disappearance from porphyry copper and other hydrothermal ore deposits. *Econ. Geol.* 103, 539–554.
- Berberian, M., King, G.C.P., 1981. Towards a paleogeography and tectonic evolution of Iran. *Can. J. Earth Sci.* 18, 210–265.
- Bonyadi, Z., Davidson, G., Mehrabi, B., Meffre, S., Ghazban, F., 2011. Significance of apatite REE depletion and monazite inclusions in the brecciated Se-Chahun iron oxide-apatite deposit, Bafq district, Iran: Insights from Paragenesis and geochemistry. *Chem. Geol.* 281, 253–269.
- Bottinga, Y., Javoy, M., 1973. Comments on oxygen isotope geothermometry. *Earth Planet Sci Lett.* 20, 250–265.
- Bottrell, S.H., Yardley, B.W.D., 1991. The distribution of Fe and Mn between chlorite and fluid: evidence from fluid inclusions. *Geochim. Cosmochim. Acta.* 55, 241–242.
- Chen, H.Y., Kyser, T.K., Clark, A.H., 2011. Contrasting fluids and reservoirs in the contiguous Marcona and Mina Justa iron oxide-Cu (-Ag-Au) deposits, south-central Peru. *Miner. Depos.* 46, 677–706.
- Chen, W.T., Zhou, M.F., 2012. Paragenesis, stable isotopes and molybdenite Re-Os isotope age of the Lala iron-copper deposit, Southwest China. *Econ. Geol.* 107, 459–480.
- Clark, T., Gobeil, A., David, J., 2005. Iron oxide-copper-gold-type and related deposits in the Manitou Lake area, eastern Grenville Province, Quebec: Variations in setting, composition, and style. *Can. J. Earth Sci.* 42, 1829–1847.
- Daliran, F., 1990. The magnetite - apatite deposit of Mishdovan, east central Iran. An alkali rhyolite hosted "Kiruna-type" occurrence in the infracambrian Bafq metallect; Ph.D. thesis, Univ. of Heidelberg. *Geowiss. Abhandl.* 37, 248 p.
- Daliran, F., 1999. REE geochemistry of Bafq apatites: Implication for the genesis of Kiruna-type iron ores; Mineral deposits; processes to processing, Stanley et al. (Eds.) Balkema, Rotterdam, 631–634.
- Daliran, F., 2002. Kiruna-type iron oxide-apatite ores and apatites of Bafq district, Iran, with an emphasis on the REE geochemistry of their apatites. PGC Publishing, Linden Park, South Australia, pp. 303–320.
- Daliran, F., Stosch, H.G., Williams, P., 2009. A review of the Early Cambrian magmatic and metasomatic events and their bearing on the genesis of the Fe oxide-REE-apatite deposits (IOA) of the Bafq District, Iran. In: Williams et al. (eds.) Smart science for exploration and mining: proceedings of the 10th Biennial SGA Meeting, Townsville, Australia, 623–625.
- Daliran, F., Stosch, H.G., Williams, P., Jamli, H., Dorri, M.B., 2010. Early Cambrian iron oxide-apatite-REE (U) deposits of the Bafq District, East Central Iran. In: Corriveau L, Mumin H (eds.) Exploring for iron oxide copper gold deposits: Canada and global analogues. *Geol. Assoc. Canada.* 20, 143–155 (Short Course Notes).
- Deymara, S., Yazdia, M., Rezvanianzadeh, M.R., Behzadi, M., 2018. Alkali metasomatism as a process for Ti-REE-Y-U-Th mineralization in the Saghand Anomaly 5, Central Iran: Insights from geochemical, mineralogical, and stable isotope data. *Ore Geol. Rev.* 93, 308–336.
- Dupuis, C., Beaudoin, G., 2011. Discriminant diagrams for iron oxide trace element finger printing of mineral deposit types. *Miner. Deposita.* 46, 319–335.
- Fisher, L.A., 2007. Hydrothermal processes at the Osborne Fe-Oxide-Cu-Au deposit, NW Queensland: Integration of multiple micro analytical data sets to trace ore fluid sources: Ph.D. Thesis, James Cook University.
- Fisher, L.A., Kendrick, M.A., 2008. Metamorphic fluid origins in the Osborne Fe oxide-Cu-Au deposit, Australia: evidence from noble gases and halogens. *Miner. Deposita.* 43, 483–497.
- Förster, H., Jafarzadeh, A., 1994. The Bafq mining district in Central Iran: a highly mineralized Infracambrian volcanic field. *Econ. Geol.* 89, 1697–1721.
- Ghahreini, G., Karimi, M., 2011. Vein type mineralization and related alteration of Narigun polymetallic deposit, east of Yazd Central Iran. *ICAM.* 10(2), 229–236.
- Gillen, D., 2010. A study of IOCG-related hydrothermal fluid in the Wernecke Mountains, Yukon Territory, Canada: Ph.D. Thesis, James Cook University, 562.
- Grainger, C.J., Groves, D.L., Tallarico, F.H.B., Fletcher, I.R., 2008. Metallogenesis of the Carajás mineral province, southern Amazon craton, Brazil: Varying styles of Archean through Paleoproterozoic to Neoproterozoic base-and precious-metal mineralization. *Ore. Geol. Rev.* 33, 451–489.
- Graupner, T., Bratz, H., Klemd, R., 2005. LA-ICP-MS micro-analysis of fluid inclusions in quartz using a commercial Merchantek 266 nm Nd:YAG laser: a pilot study. *Eur. J. Mineral.* 17, 93–102.
- Groves, D.L., Bierlein, F.P., 2007. Geodynamic settings of mineral deposit systems. *J. Geol. Soc (London, U.K.)* 164, 19–30.
- Groves, D.L., Bierlein, F.P., Meinert, L.D., Hitzman, M.W., 2010. Iron oxide copper-gold (IOCG) deposits through Earth history: implications for origin, lithospheric setting and distinction from other epigenetic iron oxide deposits. *Econ. Geol.* 105, 641–654.
- Guillong, M., Meier, D., Allan, M.M., Henrich, C.A., Yardley, B.W.D., 2008. Drift correction and data reduction were carried out with the MATLAB-based SILLS software. *Miner. Assoc. Can. Vancouver (Short course series)* 40(3) 328–333.
- Haghipour, A., 1974. Etude géologique de la région de Biabanak-Bafq (Iran Central); pétrologie et tectonique du socle Précambrien et de sa couverture (MSc Thesis) Université Scientifique et Médicale de Grenoble, France, p. 403.
- Haghipour, A., 1977. Geological Map of the Posht-e-Badam Area. Tehran, Geological Survey of Iran, scale 1 (100), 000.
- Haghipour, A., Pelissier, G., 1977. Geology of the Saghand Sector. In: Haghipour, A., Valeh, N., Pelissier, G., Davoudzadeh, M. (Eds.), Explanatory Text of the Ardekan Quadrangle Map. Geological Survey of Iran, pp. 10–68.
- Hamedji, M.A., 1995. Lower Palaeozoic sedimentology and stratigraphy of the Kerman region, East Central Iran: Ph.D. Thesis, University of Wollongong, New South Wales, Australia. 196 p.
- Hart, C.J.R., Mair, J.L., Goldfarb, R.J., Groves, D.L., 2004. Source and redox controls on metallogenic variations in ore systems, Tombstone-Tungsten Belt, Yukon, Canada: Transactions, Royal Society of Edinburgh. *Earth. Sci.* 95, 339–356.
- Heinrich, C.A., Pettko, T., Halter, W.E., Aigner-Torres, M., Audétat, A., Günther, D., Hattendorf, B., Bleiner, D., Guillong, M., Horn, I., 2003. Quantitative multi-element analysis of minerals, fluid and melt inclusions by laser-ablation inductively-coupled-plasma mass-spectrometry. *Geochim. Cosmochim. Acta.* 67, 3473–3489.
- Hitzman, M.W., 2000. Iron oxide-Cu-Au deposits: what, where, when, and why. In: Porter, T.M. (Ed.), Hydrothermal iron oxide copper-Gold and related deposits: a global perspective. PGC, Adelaide, pp. 9–25.
- Hitzman, M.W., Oreskes, N., Einaudi, M.T., 1992. Geological characteristics and tectonic setting of Proterozoic iron oxide (Cu-U-Au-REE) deposits. *Precambrian. Res.* 58, 241–287.
- Hitzman, M.W., Valenta, R.K., 2005. Uranium in iron oxide-copper-gold (IOCG) systems. *Econ. Geol.* 100, 1657–1661.
- Hoefs, J., 1987. Stable Isotope Geochemistry. Springer, Berlin Heidelberg, New York.
- Horita, J., 2014. Oxygen and carbon isotope fractionation in the system dolomite-water-CO₂ at elevated temperatures. *Geochim. Cosmochim. Acta.* 129, 111–124.
- Huckriede, R., Kursten, M., Venzlaff, H., 1962. Zur geologie des gebietes zwischen Kerman und Sagand (Iran). *Geol. Jahrb. Beih.* 51, 1–197.
- Hunt, J.A., Baker, T., Thorkelson, D.J., 2007. A review of iron oxide copper-gold deposits, with focus on the Wernecke Breccias, Yukon, Canada, as an example of a non-magmatic end member and implications for IOCG genesis and classification. *Explor. Min. Geol.* 16, 209–232.
- Jami, M., 2005. Geology, geochemistry and evolution of the Esfordi phosphate-iron deposit, Bafq area, Central Iran. Ph.D. Dissertation, University of New South Wales.
- Jami, M., Dunlop, A.C., Cohen, D.R., 2007. Fluid inclusion and stable isotope study of the Esfordi apatite-magnetite deposit, central Iran. *Econ. Geol.* 102, 1111–1128.
- Johnson, C.A., Bookstrom, A.A., Slack, J.F., 2012. Sulfur, carbon, hydrogen, and oxygen isotope geochemistry of the Idaho cobalt belt. *Econ. Geol.* 107, 1207–1221.
- Karami Shahraki, B., Mehrabi, B., 2016. Iron oxide-copper-gold (IOCG) mineralization at Jalal-Abad deposit, Northwest of Zaranj. *Iran. J. Crystallogr. Mineral.* 95, 283–296 (in Farsi with English abstract).
- Kendrick, M.A., Mark, G., Phillips, D., 2007. Mid-crustal Fluid Mixing in a Proterozoic Fe oxide-Cu-Au deposit: Evidence from Ar, Kr, Xe, Cl, Br, I, Ernest Henry, Australia: Earth Planet. Sci. Letters. 256, 328–343.
- Marschik, R., Leveille, R.A., Martin, W., 2000. La Candelaria and the Punta del Cobre district, Chile: Early Cretaceous iron oxide Cu-Au (-Zn-Ag) mineralization. In: Porter, T.M. (Ed.), Hydrothermal iron-oxide copper-gold and related deposits. A global perspective. Australian Mineral Foundation, Adelaide.
- Matsuhisa, Y., Goldsmith, J.R., Clayton, R.N., 1979. Oxygen isotopic fractionation in the system quartz-albite-anorthite-water. *Geochim. Cosmochim. Acta.* 43, 1131–1140.
- Mehrabi, B., Karimi Shahraki, B., Bazargani Guilani, K., Masoud, F., 2015. Early Cambrian high-temperature dolomite of the Rizu Series in the Jalal-Abad iron ore deposit, Central Iran. *Arab. J. Geosci.* 8, 7163–7176.
- Monteiro, L.V.S., Xavier, R.P., de Carvalho, E.R., Hitzman, M.W., Johnson, C.A., Filho, C.R.D., Torresi, I., 2008. Spatial and temporal zoning of hydrothermal alteration and

- mineralization in the Sossego iron oxide-copper gold deposit, Carajás Mineral Province, Brazil: Paragenesis and stable isotope constraints. *Miner. Deposita*. 43, 129–159.
- Moore, F., Modabberri, S., 2003. Origin of Choghart iron oxide deposit, Bafq mining district, central Iran: new isotopic and geochemical evidence. *J. Sci. IRI*. 14 (3), 259–269.
- Nabatian, G., Rastad, E., Neubauer, F., Honarmand, M., Ghaderi, M., 2015. Fe and Fe-Mn mineralization in Iran: Implications from Tethyan Metallogeny. *Australia. J. Earth Sci.* 62, 211–241.
- NISCO, 1980. Result of search and valuation works at magnetic anomalies of the Bafq iron ore region during 1976-1979, Unpub. Rep., National Iran Steel Corporation.
- Ohmoto, H., Goldhaber, M.B., 1997. Sulfur and Carbon isotopes. In: Barnes, H.L. (Ed.), *Geochemistry of hydrothermal ore deposits*, 3rd edn. Wiley, New York.
- Ohmoto, H., Rye, R.O., 1979. Isotopes of sulphur and carbon. In: Barnes, H.L. (Ed.), *Geochemistry of Hydrothermal Ore Deposits*, 2nd edition. Wiley-Inter Science, New York.
- Oreskes, N., Einaudi, M.T., 1990. Origin of rare earth element-enriched hematite breccias at the Olympic Dam Cu-U-Au-Ag deposit, Roxby Downs, South Australia. *Econ. Geol.* 85, 1–28.
- Oreskes, N., Einaudi, M.T., 1992. Origin of hydrothermal fluids at Olympic Dam: preliminary results from fluid inclusions and stable isotopes. *Econ. Geol.* 87, 64–90.
- Pollard, P.J., 2001. Sodic (calcic) alteration associated with Fe-oxide-Cu-Au deposits: an origin via unmixing of magmatic-derived H₂O-CO₂-salt fluids. *Miner. Deposita*. 36, 93–100.
- Pollard, P.J., 2006. An intrusion-related origin for Cu-Au mineralization in iron oxide-copper-gold (IOCG) provinces. *Miner. Deposita*. 41, 179–187.
- Ramezani, J., 1997. Regional geology, geochronology and geochemistry of the igneous and metamorphic rock suites of the Saghand Area, central Iran: Ph.D. Thesis, St. Louis, Missouri, Washington University. 416 p.
- Rajabi, A., Canet, C., Rastad, E., Alfonso, P., 2015. Basin evolution and stratigraphic correlation of sedimentary-exhalative Zn-Pb deposits of the Early Cambrian ZariganChahmir basin. *Central Iran. Ore Geol. Rev.* 64, 328–353.
- Ramezani, J., Tucker, R.D., 2003. The Saghand region, central Iran: U-Pb geochronology, petrogenesis and implications for Gondwana tectonics. *Am. J. Sci.* 303, 622–665.
- Rhodes, A.L., Oreskes, N., Sheets, S., 1999. Geology and rare earth element geochemistry of magnetic deposits at El Laco, Chile. *Soc. Econ. Geol. (Spec Pub)* 17, 299–332.
- Rieger, A.A., Marschik, R., Diaz, M., Hlozil, S., Chiaradia, M., Akker, B., Spangenberg, J.E., 2010. The hypogene iron oxide-copper-gold mineralization in the Mantoverde district, northern Chile. *Econ. Geol.* 105, 1271–1299.
- Roedder, E., 1984. Fluid inclusions. *Mineral. Soc. Am. Rev.*
- Ronchi, P., Masetti, D., Tassan, S., Camocino, D., 2012. Hydrothermal dolomitization in platform and basin carbonate successions during thrusting: a hydrocarbon reservoir analogue (Mesozoic of Venetian Southern Alps, Italy). *Mar and. Pet. Geol.* 29, 68–89.
- Samani, B.A., 1988. Metallogeny of the Precambrian in Iran. *Precambrian Res.* 39, 85–106.
- Samani, B.A., 1998. Precambrian metallogeny in Central Iran. *AEOI Sci. Bull.* 17, 1–16 (in Persian with English abstract).
- Samani, B.A., 1993. Saghand Formation, a riftogenic unit of upper Precambrian in central Iran. *J. Geosci.* 6, 32–45.
- Schmidt, M., Xeflide, S., Botz, R., Mann, S., 2005. Oxygen isotope fractionation during synthesis of Ca-Mg carbonate and implications for sedimentary dolomite formation. *Geochim. Cosmo. Acta.* 69, 4665–4674.
- Shepard, T.J., Rankin, A.H., Alderton, D.H.M., 1985. A practical guide to Fluid inclusion studies. Blackie.
- Shepherd, T.J., Chenery, S.R., 1995. Laser ablation ICP-MS elemental analysis of individual fluid inclusions: An evaluation study. *Geochim. Cosmochim. Acta.* 59, 3997–4007.
- Sillitoe, R.H., 2003. Iron oxide-copper-gold deposits: an Andean view. *Miner. Deposita* 38, 787–812.
- Sostaric, S.B., Palinkas, L.A., Topa, D., Spangenberg, J.E., Prochaska, W., 2011. Silver-base metal epithermal vein and listvenite types of deposit Crnac, Rogozna Mts., Kosovo. Part I: Ore mineral geochemistry and sulfur isotope study. *Ore. Geol. Rev.* 40, 65–80.
- Stoffell, B., Wilkinson, J.J., Jeffries, T.E., 2004. Metal transport and deposition in hydrothermal veins revealed by 213nm UV laser ablation microanalysis of single fluid inclusions. *Am. J. Sci.* 304, 533–557.
- Stosch, H.G., Romer, R.L., Daliran, F., 2011. Uranium-lead ages of apatite from iron oxide ores of the Bafq District, East-Central Iran. *Miner. Deposita*. 46, 9–21.
- Talbot, C.J., Alavi, M., 1996. The past of a future syntaxis across the Zagros. In: Alsop, G.L., Blundell, D.J., Davison, I. (Eds.), *Salt Tectonics*. Geological Society Special Publications, pp. 89–109.
- Taylor, B.E., 1986. Magmatic volatiles: isotopic variation of C, H, and S. *Rev. Miner.* 16, 185–225.
- Taylor, H.P., Shepard, S.M., 1986. Igneous Rocks I: Processes of isotopic fractionation and isotope systematics. In: *Stable Isotopes in High Temperature Geological Processes*, J. W. Valley, H.P. Taylor Jr. and J.R. O'Neil (eds.). *Rev. Miner.* 16, 227–269.
- Technoexport, 1976. Results of the survey of Zarand ore deposit. National Iran Steel Corporation. (Internal Report).
- Thiéry, R., Van den Kerkhof, A.M., Dubessy, J., 1994. VX properties of CH₄-CO₂ and CO₂-N₂ fluid inclusions: modeling for T < 31°C and P < 400 bars. *Eur. J. Mineral.* 6, 753–771.
- Torab, F.M., Lehmann, B., 2007. Magnetite-apatite deposits of the Bafq district, Central Iran: apatite geochemistry and monazite geo-chronology. *Mineral. Mag.* 71, 347–363.
- Vanko, D.A., Bishop, F.C., 1982. Occurrence and origin of marialitic scapolite in the Humboldt Lopolith, NW Nevada. *Contrib. Mineral. Petr.* 81, 277–289.
- Wilkinson, J.J., 2001. Fluid inclusions in hydrothermal ore deposits. *Lithos* 55, 229–272.
- Wilkinson, J.J., Stoffell, B., Wilkinson, C.C., Jeffries, T.E., Appold, M.S., 2009. Anomalously metal-rich fluids from hydrothermal ore deposits. *Science* 323, 764–767.
- Williams, P., 2010a. Classifying IOCG deposits. In: *Exploring for iron oxide copper-gold deposits: Canada and global analogues*. *Geol. Assoc. Can. (Short Course Notes)* 20, 11–19.
- Williams, P.J., Barton, M.D., Johnson, D.A., Fontbote, L., DeHaller, A., Mark, G., Oliver, N.H.S., Marschik, R., 2005. Iron oxide copper-gold deposits: geology, space-time distribution and possible modes of origin. *Econ. Geol. (100th anniversary volume)* 100 (4), 371–405.
- Whitney, D.L., Evans, D.W., 2010. Abbreviations for names of rock-forming minerals. *Am. Mineral.* 95, 185–187.
- Yardley, B.W.D., 2005. 100th Anniversary Special Paper: metal concentrations in crustal fluids and their relationship to ore formation. *Econ. Geol. (100th anniversary)* 100 (4), 613–632.
- Yardley, B.W.D., Banks, D.A., Barnicoat, A.C., 2000. The chemistry of crustal brines: tracking their origins. In: Porter, T.M. (Ed.), *Hydrothermal iron oxide copper gold and related deposits: a global perspective*. Adelaide, PGC, pp. 61–70.
- Zhao, X.F., Zhou, M.F., 2011. Fe-Cu deposits in the Kangdian region, SW China: a Proterozoic IOCG (iron-oxide-copper-gold) metallogenic province. *Miner. Deposita*. 46, 731–747.
- Zoheir, B., Akawy, A., Hassan, I., 2008. Role of fluid mixing and wall rock sulfidation in gold mineralization at the Semna minearea, central Eastern Desert of Egypt: evidence from hydrothermal alteration, fluid inclusions and stable isotope data. *Ore. Geol. Rev.* 34, 580–596.